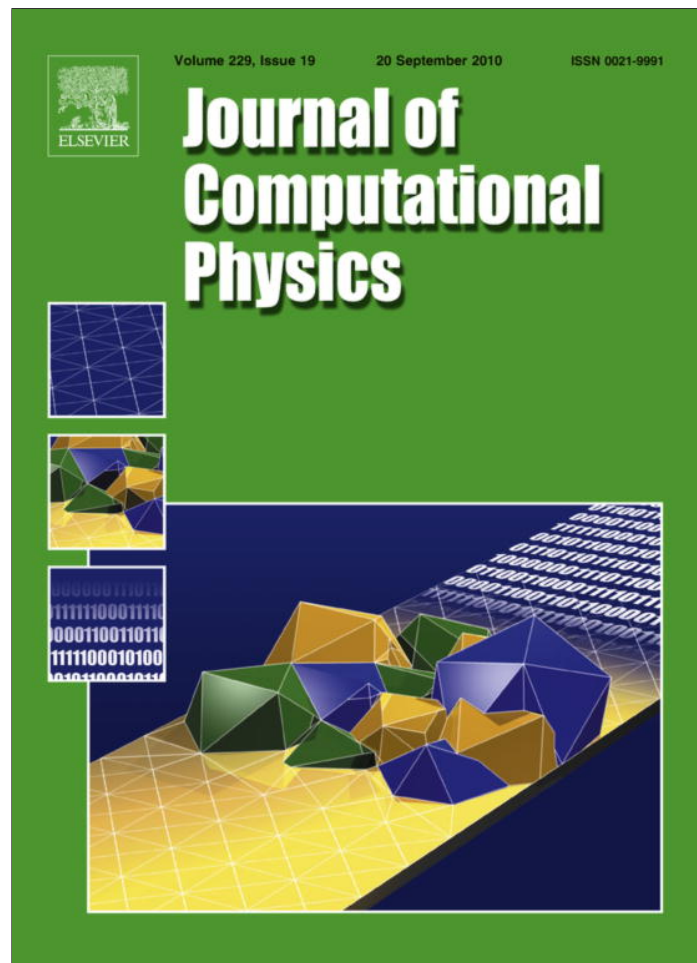


Provided for non-commercial research and education use.
Not for reproduction, distribution or commercial use.



This article appeared in a journal published by Elsevier. The attached copy is furnished to the author for internal non-commercial research and education use, including for instruction at the authors institution and sharing with colleagues.

Other uses, including reproduction and distribution, or selling or licensing copies, or posting to personal, institutional or third party websites are prohibited.

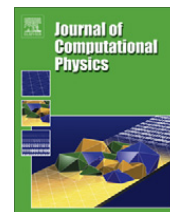
In most cases authors are permitted to post their version of the article (e.g. in Word or Tex form) to their personal website or institutional repository. Authors requiring further information regarding Elsevier's archiving and manuscript policies are encouraged to visit:

<http://www.elsevier.com/copyright>



Contents lists available at ScienceDirect

Journal of Computational Physics

journal homepage: www.elsevier.com/locate/jcp

An interface capturing method for the simulation of multi-phase compressible flows

Ratnesh K. Shukla^{a,1}, Carlos Pantano^b, Jonathan B. Freund^{b,c,*}

^a Computational Science and Engineering, University of Illinois at Urbana-Champaign, Urbana, IL 61801, USA

^b Department of Mechanical Science and Engineering, University of Illinois at Urbana-Champaign, Urbana, IL 61801, USA

^c Department of Aerospace Engineering, University of Illinois at Urbana-Champaign, Urbana, IL 61801, USA

ARTICLE INFO

Article history:

Received 4 November 2009

Received in revised form 5 May 2010

Accepted 15 June 2010

Available online 1 July 2010

Keywords:

Multi-phase flows
Phase field models
Interface capturing
Shocks

ABSTRACT

A novel finite-volume interface (contact) capturing method is presented for simulation of multi-component compressible flows with high density ratios and strong shocks. In addition, the materials on the two sides of interfaces can have significantly different equations of state. Material boundaries are identified through an interface function, which is solved in concert with the governing equations on the same mesh. For long simulations, the method relies on an interface compression technique that constrains the thickness of the diffused interface to a few grid cells throughout the simulation. This is done in the spirit of shock-capturing schemes, for which numerical dissipation effectively preserves a sharp but mesh-representable shock profile. For contact capturing, the formulation is modified so that interface representations remain sharp like captured shocks, countering their tendency to diffuse via the same numerical diffusion needed for shock-capturing. Special techniques for accurate and robust computation of interface normals and derivatives of the interface function are developed. The interface compression method is coupled to a shock-capturing compressible flow solver in a way that avoids the spurious oscillations that typically develop at material boundaries. Convergence to weak solutions of the governing equations is proved for the new contact capturing approach. Comparisons with exact Riemann problems for model one-dimensional multi-material flows show that the interface compression technique is accurate. The method employs Cartesian product stencils and, therefore, there is no inherent obstacles in multiple dimensions. Examples of two- and three-dimensional flows are also presented, including a demonstration with significantly disparate equations of state: a shock induced collapse of three-dimensional van der Waal's bubbles (air) in a stiffened equation of state liquid (water) adjacent to a Mie-Grüneisen equation of state wall (copper).

© 2010 Elsevier Inc. All rights reserved.

1. Introduction

Though there seems ever to be room for improvement, finite-volume shock-capturing methods have been remarkably successful. Nearly discontinuous shocks are effectively and robustly represented across a few mesh cells using modern methods [55]. The local structure of the characteristics in the neighborhood of a shock offers a perspective on the root reasons for this success: the convergence of the characteristics towards the shock (compression) is balanced by the numerical

* Corresponding author at: Department of Mechanical Science and Engineering, University of Illinois at Urbana-Champaign, Urbana, IL 61801, USA. Tel.: +1 (217) 244 7729; fax: +1 (217) 333 1942.

E-mail addresses: ratnesh@mecheng.iisc.ernet.in (R.K. Shukla), cpantano@illinois.edu (C. Pantano), jbfreund@illinois.edu (J.B. Freund).

¹ Present address: Department of Mechanical Engineering, Indian Institute of Science, Bangalore 560 012, India.

dissipation, which models the physical dissipation in the shock. A balance of these mechanisms maintains the shock as a relatively sharp but mesh-representable feature. Rarefactions, of course, have the opposite outward local characteristics behavior, but by their nature become better and better resolved in time and so are not easily harmed by artificial numerical dissipation. Contact discontinuities, which in the current study are of interest for material interfaces in multi-component flows, are in a way fundamentally more challenging to represent. In this case, the characteristics are parallel to the contact and so, in contrast to shocks, there is no advective balance for the numerical diffusion. As a result, any function that represents the materials, such as a density or auxiliary interface function, will diffuse in time. Thus, sharp contact discontinuities will become artificially smeared to the detriment of the numerical model. The principal contribution of this paper is a scheme for capturing a material boundary across a small number of mesh cells with similar robustness and geometric flexibility as shock-capturing schemes. This requires both maintaining a relatively sharp material boundary, which is particularly important if each material obeys a different equation of state, as well as a sharp density boundary, as would exist, say, between a gas and a liquid. In a similar spirit to the way shock-capturing can be crudely viewed as adding the dissipation needed to keep the shock acceptably resolved by the mesh, our approach is to add terms to the governing equations that play the role of an advection toward the contact, suppressing the spurious spreading caused by the same numerical dissipation needed for capturing shocks.

Our approach is based upon so-called single-fluid modeling of multi-component flows and is widely used in simulation of multi-phase compressible flows [24,42,25,1,43,44,2,47,49,22]. The term single-fluid here means that, in contrast to say ghost-fluid methods, there are no overlaid fields of different fluids. These methods effectively avoid spurious pressure oscillations that frequently occur at the multi-fluid interfaces by relaxing strict numerical conservation in favor of continuity of pressure [2], and are naturally able to handle complex topological changes, including dynamic creation of interfaces as in cavitation or chemical reaction. One major drawback associated with these algorithms, when applied to multi-phase flows, is their inability to sharply capture contact discontinuities, most importantly that between the fluids. This is particularly important where there are significant differences in the equation of state between the two fluids or large density differences. Our interface compression technique prevents the smearing of the interface during the course of computations. This has been done previously for incompressible flows [39,40,11], but these formulations do not directly translate to compressible flow. Our generalization has required significant additional development, particularly a corresponding method to maintain sharp density gradients since they are no longer tied directly to the material as in an incompressible flow.

Numerous methods have been proposed from different perspectives to treat material boundaries. Arbitrary Lagrangian–Eulerian methods [33] and free-Lagrange methods [5,56] consider multi-material interfaces as genuine discontinuities and treat them as boundaries of a distorting computational grid. Front tracking [8,14,17,15,9] attempts to exploit the advantages of both Eulerian and Lagrangian approaches: Lagrangian markers are used to identify regions occupied by different fluids for an underlying Eulerian solver. While these methods are, in a sense, the most rigorous because they strictly maintain a sharp boundary, large interface deformations and topological changes make them geometrically complex and computationally expensive, and in many cases seemingly impractical in three dimensions. In the spirit of shock-capturing, we forgo the strict precision of these Lagrangian approaches in favor of simpler methods with greater geometric flexibility.

A level-set method [41,46,35] combined with the ghost-fluid technique [12] is a popular technique, which involves extrapolation of appropriate state variables across the multi-material interface. However, this extrapolation based technique is not universal and special procedures have to be devised in order to accurately model wave-interface interactions in extreme conditions of strong shocks and high density ratios [30–32,21,52]. For example the technique that works well with gas–gas interfaces is inaccurate for water–gas interfaces and vice versa [32]. Additionally, these methods need modifications for simulating the dynamic creation of interfaces because of difficulties associated with assigning ghost cell values at newly created material boundary. Hence an isentropic single-phase cavitation model, instead of a two-fluid model that allows liquid and vapor phases to coexist [43], was employed in by Xie et al. [58] to study underwater explosion near a free surface.

Flux modification based techniques [37,38,7,6] introduce appropriate corrections to the numerical flux close to the interface in order to maintain stability and robustness. For example, a two-fluid Riemann solver can be used in combination with interpolation and extrapolation of interface fluxes in order to model wave-interface interactions [37,38]. Chang and Liou [7] and Banks et al. [6] take pressure and velocity uniformity across the contact to be the underlying principle from which to derive flux corrections near the multi-fluid interface. These modifications disrupt the conservation of the overall scheme and their derivation assumes a single fluid–fluid interface. Hence, these methods are not directly applicable to the problems of interest here in which more than two phases coexist or another phase may result from chemical reactions or phase changes.

The PDE based interface sharpening technique we develop utilizes a combination of an interface function sharpening and density correction to restrict the thickness of the numerically diffused interface. We use an interface function representing volume fraction rather than a distance function, as in a level-set description [41,46]. This approach facilitates the expressions of the thermodynamic properties of the multi-fluid mixture. Our means of capturing the contact discontinuity, both the interface function and density field, is discussed in Sections 2 and 3. This is the main contribution of the paper, and it is not directly coupled to any particular overall flow solver. The details of the multi-component compressible flow model we use and its discretization are provided in Sections 4 and 5, respectively. Results from numerical experiments showing the accuracy and stability of the proposed technique are presented in Section 6. These include liquid–gas systems with density ratios of up to 10^3 , flows with topological changes, and a three-component system with van der Waal's gas, stiffened, and

Mie-Grüneisen equations of state. A proof of the conservation properties of the scheme is provided in Section 7, before the conclusions.

2. Interface function equation

2.1. Background

In the multi-phase modeling approach discussed here, an interface function ϕ is used to distinguish between the two fluids. This function takes the values $\phi = 0$ or $\phi = 1$ in the pure fluids on either side of the interface. The generally sharp boundary between immiscible materials is modeled by the smooth variation of ϕ between these limits. With this definition, the motion of the interface is governed by an advection equation for this interface function

$$\frac{\partial \phi}{\partial t} + \mathbf{u} \cdot \nabla \phi = 0, \quad (1)$$

where \mathbf{u} is the fluid velocity. Note that this equation is strictly defined at a fixed value of ϕ , a level set that defines the interface, and is a Lagrangian statement of the movement of the material interface separating two fluids. Without additional care, numerical solutions of (1) using methods compatible with shock capturing techniques in multiple dimensions will diffuse the interface, causing the transition from $\phi = 0 \rightarrow \phi = 1$ to occur over an increasingly wider region of space as time increases.

In order to maintain a consistently sharp interface in incompressible flows, Olsson et al. [40] added an additional term to the right-hand side of (1) that restores, or regularizes, the missing immiscibility condition of the two fluids:

$$\frac{\partial \phi}{\partial t} + \mathbf{u} \cdot \nabla \phi = \mathcal{U}_o \nabla \cdot (\epsilon_h \mathbf{n} (\mathbf{n} \cdot \nabla \phi) - \phi(1 - \phi) \mathbf{n}), \quad (2)$$

where $\mathbf{n} = \nabla \phi / |\nabla \phi|$ is the local interface normal, ϵ_h is a length-scale of the order of the grid spacing, and \mathcal{U}_o is the characteristic compression velocity of the interface sharpening, much larger than $\|\mathbf{u}\|_\infty$. We are interested in small ϵ_h and large \mathcal{U}_o since this corresponds to thin material interfaces. For this case, the solution of (2) can be decomposed into fast and slow parts, the fast part governed by \mathcal{U}_o and the slow by the local velocity \mathbf{u} . In one space dimension, the fast solution is

$$\phi = \frac{1}{1 + \exp\left(-\frac{n}{\epsilon_h}\right)} = \frac{1}{2} \left(1 + \tanh\left(\frac{n}{2\epsilon_h}\right) \right), \quad (3)$$

where n denotes the spatial coordinate normal to the interface with respect to the center of the interface, $\phi = 1/2$. The correction term on the right-hand side of (2) combines diffusive and compressive fluxes such that the interface thickness remains approximately proportional to ϵ_h , where ϵ_h is small. Note that the correction term is only non-zero for $0 < \phi < 1$, so (2) reverts back to (1) under simultaneous refinement of the mesh and ϵ_h (see Section 7). Moreover, the actual value of \mathcal{U}_o is immaterial in practice since when it is sufficiently large (3) is independent of \mathcal{U}_o .

2.2. Reformulation

The idea behind (2), where the one-dimensional solution is (3), can be generalized to multiple dimensions in several ways. The divergence form in (2), originally proposed by Olsson et al. [40], is just one possibility. Another possibility is to project the gradient of

$$K = \epsilon_h |\nabla \phi| - \phi(1 - \phi), \quad (4)$$

in the normal direction, giving

$$\frac{\partial \phi}{\partial t} + \mathbf{u} \cdot \nabla \phi = \mathcal{U}_o \mathbf{n} \cdot \nabla (\epsilon_h |\nabla \phi| - \phi(1 - \phi)). \quad (5)$$

In one dimension there is no difference between (2) and (5) because $\mathbf{n} = \pm 1$. It will be shown that the multidimensional form (2) does not perform as well as the one-dimensional version and we propose an improvement to alleviate the observed problems and generalize to compressible flow.

One can anticipate that the compression term in (2) can potentially yield spurious behavior under some circumstances by considering

$$\nabla \cdot (\epsilon_h \mathbf{n} (\mathbf{n} \cdot \nabla \phi) - \phi(1 - \phi) \mathbf{n}) = K(\nabla \cdot \mathbf{n}) + \mathbf{n} \cdot \nabla K = K(\nabla \cdot \mathbf{n}) + \frac{\partial K}{\partial n}. \quad (6)$$

In the limit $\mathcal{U}_o \rightarrow \infty$, $K = 0$ and the profile (3) results. However, for finite \mathcal{U}_o and finite grid resolution, $K \neq 0$. In this case, (6) implies that the interface is being changed both normally and tangentially depending on the strength and accuracy of the curvature evaluation, $\nabla \cdot \mathbf{n}$. Further discussion and demonstration calculations are provided below.

Finally, in incompressible flow applications the velocity field is solenoidal and the advection term in (2) can be rewritten in conservation form $\nabla \cdot (\phi \mathbf{u})$. This allows immediate discrete mass conservation using the standard, flux-based,

discretization practice. In compressible flow applications, it is best to craft (2) or (5) in an appropriate conservation form using the mass conservation equation for one of the fluids, giving

$$\frac{\partial(\rho_1\phi)}{\partial t} + \nabla \cdot (\rho_1\phi\mathbf{u}) = \rho_1\mathcal{U}_o\mathbf{n} \cdot \nabla(\epsilon_h|\nabla\phi| - \phi(1-\phi)), \quad (7)$$

where ρ_1 is the density of the fluid labeled '1', see Section 4.

2.3. Calculation of normals

As in the case of shocks, the representation of sharp physical interfaces by our model is most realistic if their thickness is minimized. This corresponds to taking ϵ_h as small as possible. However, accurate computation of the gradients of ϕ , including those that define \mathbf{n} , are well-behaved only if ϕ is sufficiently resolved on the computational mesh. Otherwise, numerical artifacts appear and quickly disrupt the attractive properties of (2). This is counter to the modeling objective of maintaining a sharp interface. A similar situation led Desjardins et al. [11] to propose an alternative method for calculation of interface normals, which are particularly important for evaluating the right-hand side of (7). In their method, the distance function d is computed from ϕ using

$$\phi = \frac{1}{1 + \exp\left(\frac{d}{\epsilon_h}\right)}, \quad (8)$$

for points close to the interface. Away from the interface, where ϕ is either one or zero, it is not possible to compute d from ϕ using (8). Therefore, the Fast Marching Method [46] was employed to construct a distance function for points away from the interface, which was subsequently utilized to determine the normals. An alternative and less demanding approach is to avoid using ϕ directly when computing \mathbf{n} and, instead, use an auxiliary function $\psi(\phi)$, which is designed to have the same normal but which is smoother for better estimates of its gradients. We obtained good results with

$$\psi = \frac{\phi^\alpha}{\phi^\alpha + (1-\phi)^\alpha}, \quad \text{for } \alpha < 1. \quad (9)$$

The width of the hyperbolic tangent profile for ψ is $1/\alpha$ times that of ϕ . As shown in Appendix A, a small value of α will alleviate the problems associated with resolving the steep gradients of ϕ . This approach can be used in multiple dimensions by taking the gradient of both sides of (9) and solving for $\nabla\phi$, giving

$$\nabla\phi = \frac{\nabla\psi}{\alpha}(\phi(1-\phi))^{1-\alpha}(\phi^\alpha + (1-\phi)^\alpha)^2, \quad (10)$$

which is then used to calculate $\mathbf{n} = \nabla\phi/|\nabla\phi| = \nabla\psi/|\nabla\psi|$. Fig. 1 shows example contours of ϕ and ψ , computed using $\alpha = 0.1$ and $\epsilon_h = 0.5h$, for one of the two lobes that results from fragmentation of a cylindrical helium bubble in the example of Section 2.4 (see Fig. 2).

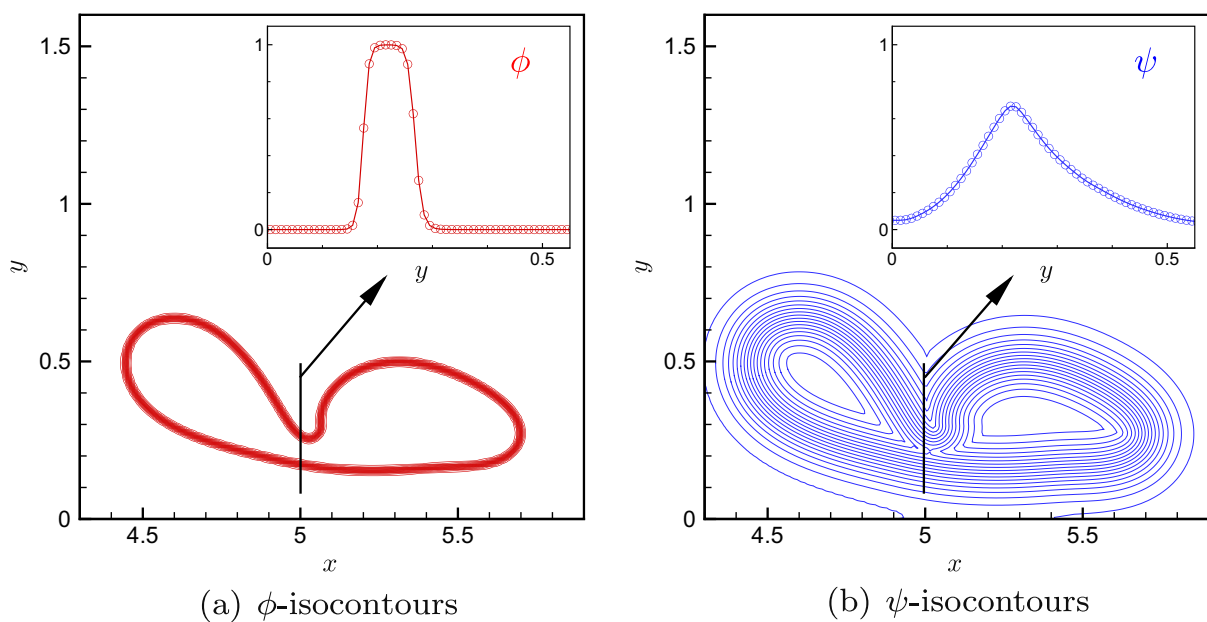


Fig. 1. Isolvels of ϕ and ψ (for $\alpha = 0.1$) computed for the air–helium shock–bubble interaction considered in Section 2.4. Inset depicts the functions along the line $x = 5.0$.

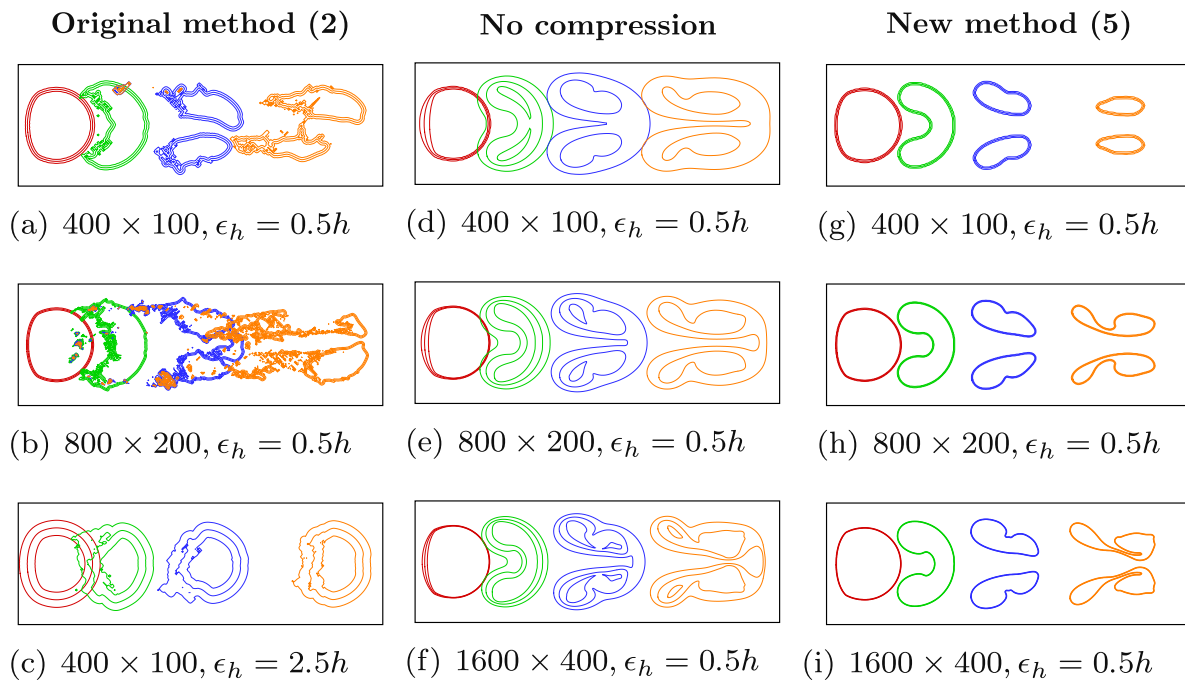


Fig. 2. Interface function contours as a function of time for Mach 1.22 air–helium shock–bubble interaction computed using the conservative interface function method given by (2) (left), no interface compression (center), and modified interface function method given by (5) (right).

The mapping (9) is clearly such that the isopleth defining the interface is unchanged by the nonlinear mapping of ϕ to ψ . We can expect that finite-difference computation of \mathbf{n} will be more accurate based upon ψ than ϕ simply because ψ is smoother and therefore its numerical differentiation yields smaller truncation errors. A general proof of this is provided in Appendix A, with specific expressions evaluated for the current second-order scheme, where an error bound is developed. Small α reduces errors associated with planar ($\sim\alpha^2$) and regular ($\sim\alpha$) curvature terms. Errors associated with second-order curvature is not reduced as $\alpha \rightarrow 0$, but these terms will be small for well resolved and sufficiently smooth interface shapes.

It is important to note that ψ becomes constant $\psi \rightarrow 0.5$ as $\alpha \rightarrow 0$. For this reason, too small α will suffer from round-off errors that will be dominant, irrespective of the value of ϕ . In this case, the advantage of using ψ in place of ϕ is lost. Our choice of $\alpha = 0.1$ ensures that the relative error in computation of normals from the mesh-representable auxiliary function ψ remains less than 1%.

2.4. Demonstration

For general compressible flows involving interactions of shock waves with multi-fluid interfaces, the application of the interface compression scheme (2) can give rise to oscillations in ϕ . To demonstrate this problem we simulate an air–helium shock–bubble interaction, which is a common test case [42,22,12,6,18,34]. A standard multi-fluid compressible flow model and TVD finite-volume shock-capturing method are used; discussed in more detail in Sections 4 and 5, respectively. Calculations are carried out using (2) and the modified interface function method (5) along with a density correction technique described in the next section. The results obtained from the two methods are shown in Fig. 2 along with those obtained without any interface compression. We see that the original method develops fine-scale oscillations, which continue to grow in time and corrupt the solution. As evident in Fig. 2, these spurious features persist with increased grid resolution (Fig. 2(b)) and increased interface thickness ϵ_h (Fig. 2(c)). As depicted in Fig. 2(d)–(f), simulations which do not use interface compression continue to diffuse the interface function in time, irrespective of the grid resolution. In contrast, computations utilizing the new modified interface method are oscillation free and remain smooth even after the interface breaks up (Fig. 2(g)–(i)). Moreover, the new formulation appears to show well-behaved convergence as the mesh is refined. Further assessment of the method is provided in Section 6, after we discuss the full scheme in the following sections.

One could argue that it should be possible to achieve discrete conservation by using (2) provided errors (such as those depicted in Fig. 2) are reduced and kept under control by using more accurate schemes for discretizing it. However, more accurate schemes which are based on higher-order discretization (WENO, HOUC) are not TVD. Application of such schemes results in spurious oscillations so that the volume fraction ϕ does not remain bounded and attains values that are less than zero and greater than one. The spurious oscillations generated by more accurate schemes leads to a loss of robustness through creation of unphysical thermodynamic states, which limits their applicability to multi-phase compressible flows. The target applications of this paper involve large density variations and strong shocks, and it is important to ensure that both advection and interface compression discretizations do not produce new extrema in ϕ . In order to achieve this objective

we have utilized a TVD based advection method for ϕ . As shown in Section 5.2 our interface compression method does not generate spurious oscillations in ϕ and ρ .

3. Density correction

For incompressible flows, where this type of interface sharpening has been applied in the past [40], the density of each fluid is fixed and thus uniquely set by ϕ . In the present case of compressible flow, the fluid density ρ will in general vary independently of ϕ , which only serves to distinguish the materials across interfaces. Neither of these alone is sufficient to uniquely determine the interface location and the fluid density. However, like ϕ , ρ gradients at interfaces will also diffuse in time, and it is desirable to suppress this for the same reasons that we sought means of suppressing the diffusion of ϕ . Following the approach for ϕ , we will identify means of modifying the density equation,

$$\frac{\partial \rho}{\partial t} + \nabla \cdot (\rho \mathbf{u}) = 0, \quad (11)$$

to suppress artificial mass diffusion. Velocity and pressure are, of course, also subject to numerical diffusion, but these are both continuous across contacts and so do not require any special treatment outside the standard techniques for capturing shocks.

Ideally, one would like to obtain the same steep profile for ρ as for the sharpened ϕ , but this is fundamentally more difficult because ρ does not have prescribed values away from the interface. A ρ equation analogous to (5) might provide a reasonable model for liquids, for which the density will not change much, but for a collapsing gas bubble, the density away from the interface changes by orders of magnitude. Therefore, suppression of numerical thickening of the density at the contact surface needs to be done in a way that is insensitive to the density values in the vicinity of the interface. With the interface already determined by ϕ , we can stipulate that ρ and ϕ gradients normal to interface are related:

$$\rho_n = \mathbf{n} \cdot \nabla \rho = C \phi_n, \quad (12)$$

where C is some scalar. This relationship is exact when ρ is constant on each side of the interface, since $\rho = \rho_1 \phi + \rho_2(1 - \phi)$, where ρ_1 and ρ_2 denote densities of the two fluids. Assuming (12) is thus tantamount to assuming that the density gradient in the smoothed representation of the material boundary is much greater than the density gradients in either of the two materials, which corresponds precisely to the situation where the density interface would be better modeled if sharpened. Taking a derivative of (12) in the n direction and multiplying by ϵ_n , we have

$$\epsilon_n \rho_{nn} = \epsilon_n C \phi_{nn} = C(\epsilon_n \phi_n)_n. \quad (13)$$

As will be confirmed in Section 7, K in (4) approaches zero for large \mathcal{U}_o . Therefore, we can assume $K \approx 0$ and differentiate (4) with respect to n such that $(\epsilon_n \phi_n)_n \approx (\phi(1 - \phi))_n$, and after replacing the last term in the right-hand side of (13) obtain

$$\epsilon_n \rho_{nn} = C(\phi(1 - \phi))_n = (1 - 2\phi)C\phi_n = (1 - 2\phi)\rho_n. \quad (14)$$

Using this analogous relationship to (5), yields an interface compression technique for the mass conservation equation:

$$\frac{\partial \rho}{\partial t} + \nabla \cdot (\rho \mathbf{u}) = H(\phi) \mathcal{U}_o \mathbf{n} \cdot (\nabla(\epsilon_n \mathbf{n} \cdot \nabla \rho) - (1 - 2\phi)\nabla \rho). \quad (15)$$

When $\rho_n = C\phi_n$, the right-hand side of this equation is clearly zero, otherwise the right-hand side guides ρ toward this condition without requiring known values for the density on each side of the interface. For compressible flow, ρ needs to evolve independently of ϕ outside the compressed region, so we localize the compression to the interface region with the $H(\phi)$ function in (15). Our numerical experiments indicate that

$$H(\phi) = \tanh \left[\left(\frac{\phi(1 - \phi)}{10^{-2}} \right)^2 \right] \quad (16)$$

is effective.

Interface density sharpening is demonstrated for the flow shown in Fig. 3. A 40 MPa shock collapses a 4 mm diameter cylindrical air cavity in water. The initial densities of air and water are 1 kg/m^3 and 1000 kg/m^3 , respectively, both at an initial pressure of 101.3 kPa. Three different simulations, performed using the same resolution (160 points across the initial bubble) and the same underlying compressible flow solver described in Section 5, are compared: one with no special treatment of the interface, one with just ϕ sharpening, and one with both ϕ and ρ sharpening. The results are shown in Fig. 4. Without interface compression, ϕ and ρ erroneously diffuse the interface throughout the domain (Fig. 4(a) and (d)). The computation that sharpens only the interface function also results in a qualitatively incorrect behavior: the density field is clearly smeared, but there is also an unexpected dimple on the trailing edge of the bubble (Fig. 4(b) and (e)). The cause of this is clear in this particular case. The water density, which is high, diffuses into the low density gas bubble, where it becomes labeled according to ϕ as a gas. Such numerical diffusion might be acceptable in some circumstances, but here the bubble is strongly compressed assuming an ideal gas equation of state. Thus, the somewhat high density in the gas due to the diffused density of the liquid is accentuated many fold, yielding a local density that is many times that of the

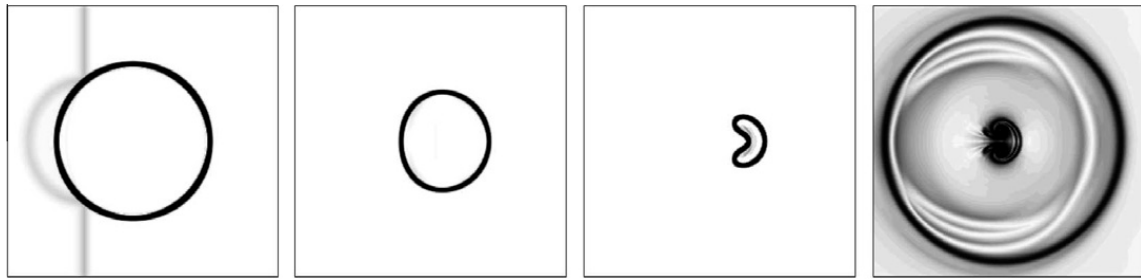


Fig. 3. Normalized density gradient contours for collapse of a cylindrical air cavity in water after it is impulsively accelerated by a planar shock with ratio of 400. Times shown are 10, 20, 30 and 35 μs after the shock first encountered the cavity.

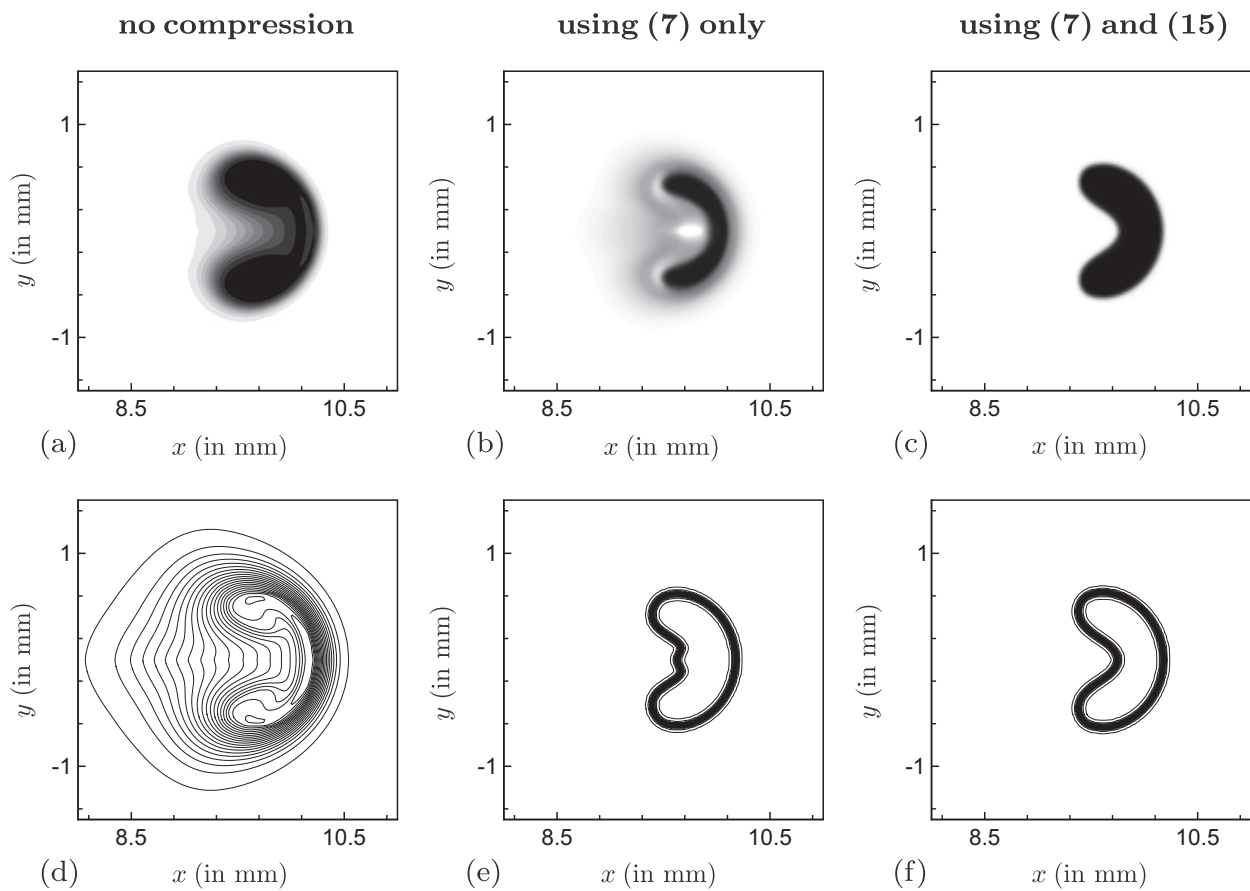


Fig. 4. Density (top) and interface function (bottom) contours at 30 μs for shock induced collapse of air cavity in water using (left) no interface compression, (center) interface function compression only and, (right) both interface function compression and density correction.

water. The inertia of this high density “spot” suppresses its acceleration relative to the rest of the bubble and leads to the peculiar shape at the trailing edge. Computations using the modified interface function method and the density compression yield density and interface function profiles that are consistent with each other (Fig. 4(c) and (f)) and without the spurious trailing edge dimple.

4. Multi-fluid compressible flow model

The previous section discussed the interface capturing aspects of the algorithm. These are coupled with a standard five equation quasi-conservative model for three-dimensional compressible two-fluid flow:

$$\frac{\partial(\rho_1 \phi)}{\partial t} + \nabla \cdot (\rho_1 \phi \mathbf{u}) = 0, \tag{17a}$$

$$\frac{\partial(\rho_2(1 - \phi))}{\partial t} + \nabla \cdot (\rho_2(1 - \phi) \mathbf{u}) = 0, \tag{17b}$$

$$\frac{\partial(\rho \mathbf{u})}{\partial t} + \nabla \cdot (\rho \mathbf{u} \mathbf{u}) + \nabla P = 0, \tag{17c}$$

$$\frac{\partial E}{\partial t} + \nabla \cdot ((E + P) \mathbf{u}) = 0, \tag{17d}$$

$$\frac{\partial \phi}{\partial t} + \mathbf{u} \cdot \nabla \phi = 0. \tag{17e}$$

The two fluids (1 and 2) are represented in terms of the volume fraction (phase field) of fluid 1, ϕ , with densities ρ_1 and ρ_2 , respectively, and velocity $\mathbf{u} = (u, v, w)^T$ in the x, y, z directions. The total energy, E , is given by [3] along with appropriate initial and boundary conditions. The total energy is related to the specific internal energy, e , according to $E = \rho e + \frac{1}{2} \rho (u^2 + v^2 + w^2)$, where $\rho = \rho_1 \phi + \rho_2 (1 - \phi)$ is the density of the mixture. The two components at any point are assumed to have the same velocity. This five equation model can be derived from the more general compressible two-fluid models, which take into account pressure non-equilibrium effects [4,23,36,45]. The effects of viscosity, surface tension, heat conduction and mass diffusion are neglected, though we have included viscosity for a particular application [13]. Bubble collapse and other shock–interface interaction problems considered in this paper typically involve high Weber numbers, and surface tension is not expected to play an important role in the overall dynamics. Johnsen and Colonius[57], for example, calculate the Weber numbers in the range 10^3 – 10^4 based on maximum jet velocity and jet size for collapse of a 10 μm bubble in water by a pressure ratio of 71.

An equation of state is required to close the equations. We assume general equation of state relationships for the two fluids $\rho_i e_i = \rho_i e_i(\rho_i, P_i)$ for $i = 1, 2$, with $\rho e = \phi \rho_1 e_1 + (1 - \phi) \rho_2 e_2$ and total pressure $P = \phi P_1 + (1 - \phi) P_2$. A relationship for the mixture equation of state of the form $P = P(\phi, \rho_1 \phi, \rho_2 (1 - \phi), \rho e)$ is also needed. Following previous analysis by Allaire et al. [3] we assume an isobaric closure, which yields

$$P_1(\rho_1, \rho_1 e_1) = P_2(\rho_2, \rho_2 e_2) = P, \tag{18a}$$

$$\phi \rho_1 e_1 + (1 - \phi) \rho_2 e_2 = \rho e. \tag{18b}$$

Simultaneous solution of (18a) and (18b) gives the pressure P for the mixture in terms of volume fraction, mass fraction, and total energy of the mixture. While a general expression for the mixture pressure P can not always be derived, a closed form relationship can be obtained when the two phases are modeled using a Mie–Grüneisen equation of state, which is fairly flexible. Thus we have $P_i(\rho_i, \rho_i e_i) = [\gamma_i(\rho_i) - 1] \rho_i e_i - \gamma_i(\rho_i) P_i^\infty(\rho_i)$ for $i = 1, 2$ along with mixture rules:

$$P = (\gamma - 1) \rho e - \gamma P^\infty, \tag{19a}$$

$$\frac{1}{\gamma - 1} = \frac{\phi}{\gamma_1(\rho_1) - 1} + \frac{1 - \phi}{\gamma_2(\rho_2) - 1}, \tag{19b}$$

$$P^\infty = \frac{\gamma - 1}{\gamma} \left(\phi \frac{\gamma_1(\rho_1) P_1^\infty(\rho_1)}{\gamma_1(\rho_1) - 1} + (1 - \phi) \frac{\gamma_2(\rho_2) P_2^\infty(\rho_2)}{\gamma_2(\rho_2) - 1} \right). \tag{19c}$$

It can be shown that the five equation model reduces to a four equation model given by (11), (17c), (17d), and (17e) when the two phases are governed by the stiffened equation of state, which can also be parameterized to model an ideal gas. This model has been used successfully in the analysis of shock–interface interactions in previous work [1,44,47,22,13]. Though we use it in demonstration simulations in Section 6, its details are not instructive for the present objectives and for brevity the detailed analysis of the five equation model is not presented here. We refer readers to references containing its full details [3,36,45]. We also mention that the application of this interface model is not restricted to the particular equations of state used in our demonstration made in this work; the general formulation has been shown to be successful when applied to more complicated or even tabulated equations of state [3]. The complete model, including interface compression, is given by (17a), (17b), (17c), (17d), (5) and (15).

In order for the interface compression technique to achieve its goal, \mathcal{U}_o must be large. This implies that the correction terms introduce numerical stiffness and appropriate time integration techniques are needed. In the present applications, we use a time splitting technique, whereby the density and interface function equations are split into an advection stage

$$\begin{aligned} \rho_t + \nabla \cdot (\rho \mathbf{u}) &= 0, \\ (\rho_1 \phi)_t + \nabla \cdot (\rho_1 \mathbf{u} \phi) &= 0, \end{aligned}$$

solved using a standard approximate Riemann solver method, followed by a compression step,

$$\rho_\tau = H(\phi) \mathbf{n} \cdot (\nabla(\epsilon_h \mathbf{n} \cdot \nabla \rho) - (1 - 2\phi) \nabla \rho), \tag{20}$$

$$\phi_\tau = \mathbf{n} \cdot \nabla(\epsilon_h |\nabla \phi| - \phi(1 - \phi)), \tag{21}$$

in pseudo-time $\tau = t \mathcal{U}_o$ (having units of length-scale). The latter is advanced to equilibrium with a substep $\Delta \tau$ and the spatial derivatives use a centered second-order accurate finite-volume discretization. For the demonstration simulations, we took $\Delta \tau = 0.2h$. Note that integrating (20) and (21) to a τ -steady state is consistent with $\mathcal{U}_o \rightarrow \infty$, a specific value of \mathcal{U}_o is not required for this solution method.

5. Numerical discretization

5.1. Compressible flow solver

For our demonstration simulations, the governing equations are discretized on a uniform fixed Cartesian mesh with equal spacing in all coordinate directions: $\Delta x = \Delta y = \Delta z = h$ and N_x , N_y , and N_z points in the x , y , and z directions, respectively. We follow the common reconstruct-and-evolve strategy within a finite-volume framework as described elsewhere [55,29]. We employ a TVD reconstruction with the Minmod limiter [29,55]. In the present work, we use the HLLC approximate Riemann solver for its good resolution of shocks and its positivity of density and internal energy [54]. Upwind fluxes for the advection equation for interface function (17e) are calculated as a part of the two-fluid Riemann problem using the contact velocity from HLLC solver. Time integration is performed using a strong-stability-preserving third-order Runge–Kutta method [16]. All demonstration simulations were advanced with a CFL time step criterion of 0.3. Note that this choice of CFL number is just a conservative one and all the test cases presented in the paper run stably with a CFL number of 1.0. Additionally, the interface compression technique is general and can be easily combined with other time integration methods [13].

At this point we also mention that multidimensional shock-capturing methods based on solution of the normal direction Riemann problems can fail due to numerical instability when high shear rates are involved [44,48]. This is linked to the fact that methods based on solution of normal Riemann problems (HLLC, or exact Godunov) may not add sufficient numerical dissipation to the tangential velocity field, which is treated as a passive scalar. This indeed can be a problem, but it is associated with the Riemann solver and is therefore distinct from the objectives of this paper. Cures to this problem involve construction of more robust Riemann solvers, and its investigation is beyond the scope of this paper.

5.2. Discretization of the phase field equation and density correction

The pseudo-time evolution of the compression algorithm, (20) and (21), use a standard second-order method, according to

$$\frac{d\phi_{ijk}}{d\tau} = -n_{ijk}^x \left(\frac{f_{i+1/2,jk} - \bar{f}_{i-1/2,jk}}{\Delta x} \right) - n_{ijk}^y \left(\frac{g_{i,j+1/2,k} - \bar{g}_{i,j-1/2,k}}{\Delta y} \right) - n_{ijk}^z \left(\frac{h_{i,j,k+1/2} - \bar{h}_{i,j,k-1/2}}{\Delta z} \right), \quad (22)$$

$$\begin{aligned} \frac{d\rho_{ijk}}{d\tau} = & -(1 - 2\phi_{ijk}) \left(n_{ijk}^x \frac{\rho_{i+1,j,k} - \rho_{i-1,j,k}}{2\Delta x} + n_{ijk}^y \frac{\rho_{i,j+1,k} - \rho_{i,j-1,k}}{2\Delta y} + n_{ijk}^z \frac{\rho_{i,j,k+1} - \rho_{i,j,k-1}}{2\Delta z} \right) - n_{ijk}^x \left(\frac{\bar{f}_{i+1/2,jk} - \bar{f}_{i-1/2,jk}}{\Delta x} \right) \\ & - n_{ijk}^y \left(\frac{\bar{g}_{i,j+1/2,k} - \bar{g}_{i,j-1/2,k}}{\Delta y} \right) - n_{ijk}^z \left(\frac{\bar{h}_{i,j,k+1/2} - \bar{h}_{i,j,k-1/2}}{\Delta z} \right), \end{aligned} \quad (23)$$

where the indexes of the discretized cells are denoted by i, j, k , the normal vector is given by $\mathbf{n}_{ijk} = (n_{ijk}^x, n_{ijk}^y, n_{ijk}^z)$, where

$$\mathbf{n}_{ijk} = \frac{(\nabla\psi)_{ijk}}{|(\nabla\psi)_{ijk}|},$$

and

$$(\nabla\psi)_{ijk} = \left(\frac{\psi_{i+1,jk} - \psi_{i-1,jk}}{2\Delta x}, \frac{\psi_{i,j+1,k} - \psi_{i,j-1,k}}{2\Delta y}, \frac{\psi_{i,j,k+1} - \psi_{i,j,k-1}}{2\Delta z} \right).$$

The compression fluxes f and \bar{f} in the x direction at the $(i + 1/2, j, k)$ cell faces are computed using

$$\begin{aligned} f_{i+1/2,jk} &= (\phi(1 - \phi))_{i+1/2,jk} - \epsilon_h (|\nabla\phi|_{i+1/2,jk}), \\ \bar{f}_{i+1/2,jk} &= -\epsilon_h \left(\frac{\nabla\phi_{i+1/2,jk} \cdot \nabla\rho_{i+1/2,jk}}{|\nabla\phi|_{i+1/2,jk}} \right), \end{aligned}$$

where

$$\begin{aligned} [\phi(1 - \phi)]_{i+1/2,jk} &= \phi_{i+1/2,jk}(1 - \phi_{i+1/2,jk}), \\ \phi_{i+1/2,jk} &= \frac{\phi_{i+1,jk} + \phi_{ijk}}{2}, \end{aligned}$$

and $\nabla\phi_{i+1/2,jk}$ is computed from $\nabla\psi_{i+1/2,jk}$ using (10). These derivatives in turn are approximated as

$$\begin{aligned} (\psi_x)_{i+1/2,jk} &= \frac{\psi_{i+1,jk} - \psi_{ijk}}{\Delta x}, \\ (\psi_y)_{i+1/2,jk} &= \frac{\psi_{i+1,j+1,k} - \psi_{i+1,j-1,k} + \psi_{i,j+1,k} - \psi_{i,j-1,k}}{4\Delta y}, \\ (\psi_z)_{i+1/2,jk} &= \frac{\psi_{i+1,j,k+1} - \psi_{i+1,j,k-1} + \psi_{i,j,k+1} - \psi_{i,j,k-1}}{4\Delta z}. \end{aligned}$$

Similarly, the compression fluxes in the y direction, g and \bar{g} , and in the z direction, h and \bar{h} , and the necessary density gradients are computed by the corresponding permutation of indices corresponding to the coordinate direction being considered. The stopping criteria for the pseudo-time integration requires that the L_∞ norm of the relative variation of ϕ and ρ be less than 10^{-6} . A condition that is satisfied after 5–10 iterations.

An important question of interest is whether the density compression (20) is capable of producing new local maxima or minima, which might degrade the overall quality of the solution. The particular concern, of course, is that the density should remain positive, which is easily violated at high density ratio interfaces unless special attention is given to the discretization. However, for the compression term we propose, this attractive property only requires that $\epsilon_h \geq 0.5h$, where h denotes the grid spacing. To show this, at least in one dimension, we consider (20) using the second-order accurate approximations described above and first-order time integration with pseudo-time index m , giving

$$\rho_i^{m+1} = \rho_i^m - C_{i-1}^m (\rho_i^m - \rho_{i-1}^m) + D_i^m (\rho_{i+1}^m - \rho_i^m), \tag{24}$$

where

$$C_{i-1}^m = \frac{\epsilon_h}{h^2} \Delta\tau H_i + \frac{(1 - 2\phi_i)}{2h} \Delta\tau H_i n_i, \tag{25}$$

$$D_i^m = \frac{\epsilon_h}{h^2} \Delta\tau H_i - \frac{(1 - 2\phi_i)}{2h} \Delta\tau H_i n_i \tag{26}$$

with $H_i = H(\phi_i)$ and $n_i = \text{sgn}(\phi_{i+1} - \phi_{i-1})$. The scheme is positivity preserving (TVD), if $C_{i-1} \geq 0$, $D_i \geq 0$, and $C_i + D_i \leq 1 \forall i$ ([20] and Theorem 6.1 from [29]), i.e.

$$\frac{\epsilon_h}{h} + n_i \frac{1 - 2\phi_i}{2} \geq 0 \tag{27}$$

$$\frac{\epsilon_h}{h} - n_i \frac{1 - 2\phi_i}{2} \geq 0, \tag{28}$$

$$\Delta\tau \left\{ \frac{\epsilon_h(H_i + H_{i+1})}{h^2} + \frac{1 - 2\phi_{i+1}}{2h} H_{i+1} n_{i+1} - \frac{1 - 2\phi_i}{2h} H_i n_i \right\} \leq 1, \tag{29}$$

Since $H_i > 0$, $-1 \leq 1 - 2\phi_i \leq 1$, and $n_i = 1$ or -1 , $\epsilon_h \geq 0.5h$ is needed for the scheme to be TVD. A limit on the pseudo-time step is also found using this same theorem, $\Delta\tau \leq h^2/(h + 2\epsilon_h)$, which given the restriction on ϵ_h implies $\Delta\tau \leq h/2$. In forming these inequalities, we recognize that the maximum value of H_i is unity. Using the generalized form of Theorem 6.1 from [29] in which coefficients C_i, D_i can be a function of ϕ_i it can be shown that the interface compression technique given by (5) is also monotonic if $\epsilon_h \geq 0.5h$. The proof is very similar to the one described above and is not presented here for brevity. Thus, both the interface compression and the density correction techniques introduced in Sections 2 and 3 are TVD provided $\epsilon_h \geq 0.5h$.

Finally, interface compression alters the density and interface function and the resulting flow field will not satisfy the condition of uniform pressure and velocity across the multi-material interface. This can have deleterious effects when strong shocks encounter interfaces with significant changes in equation of state. In general, it would be necessary to modify all the state variables, in accordance with the altered density and interface function, to enforce continuity of pressure and velocity. In our implementation, this task is accomplished by first computing primitive variables before applying the interface compression technique. The parameters in the equation of state relationship are then computed using the modified interface function in order to estimate conserved variables. The complete compressible multi-component flow algorithm with conservative vector of state $\mathbf{U} = (\rho, \rho\phi, \rho u, \rho v, \rho w, E)$ from time step l to $l + 1$ is summarized as follows:

- (i) Compute left and right states at cell faces $\mathbf{U}_L, \mathbf{U}_R$ from the cell centered values \mathbf{U}^l .
- (ii) Compute fluxes using the HLLC approximate Riemann solver and update the conserved variables from \mathbf{U}^l to \mathbf{U}^* .
- (iii) Compute primitive variables (ρ, u, v, w, P, ϕ) from conserved variables \mathbf{U}^* .
- (iv) Iterate interface function equation and density compression to τ -steady state (until the convergence criteria is satisfied), m -iterations.
- (v) Define conserved variables at the end of the time step, \mathbf{U}^{l+1} , from primitive variables of \mathbf{U}^* and the new values of ρ and ϕ function from (iv).

6. Demonstration calculations and additional discussion

In this section we begin by demonstrating the technique on one-dimensional Riemann problems for which exact analytical solutions are available. This is followed by simulations of two-dimensional shock–interface interactions. The method is subsequently applied to a three-dimensional bubble collapse adjacent a model wall. Several examples are shown to demonstrate that the same algorithm, without adjustments, can be used to simulate a range of different conditions. Following the analysis detailed in the preceding section, the parameters $\alpha = 0.1$ and $\epsilon_h = h/2$ are used in all the test cases. Outflow boundary conditions are approximated by using ghost cells with values extrapolated from appropriate adjacent interior cells [29]. Reflecting boundary conditions at solid walls are modeled in a similar way except that the sign of momentum in the wall normal direction is reversed.

6.1. One-dimensional tests

6.1.1. Air–helium interaction

Following [2], we consider a stiff two-fluid one-dimensional Riemann problem with initial condition

$$\begin{aligned}
 (\rho, u, P) &= \begin{cases} (1, 0, 500) & \text{for } 0 \leq x \leq 0.5, \\ (1, 0, 0.2) & \text{for } 0.5 < x \leq 1, \end{cases} \\
 \phi &= \frac{1}{2} \left(1 + \tanh \left(\frac{x - 0.5}{2\epsilon_h} \right) \right), \\
 \gamma &= 1 + \frac{(\gamma_2 - 1)(\gamma_1 - 1)}{\phi(\gamma_1 - 1) + (1 - \phi)(\gamma_2 - 1)},
 \end{aligned} \tag{30}$$

where the specific heat ratio of air and helium are $\gamma_1 = 1.4$, and $\gamma_2 = 1.6$, respectively. Solutions to this problem are computed both with and without interface compression on a uniform grid with 800 grid points, and the results are plotted in Fig. 5. We note that the solutions computed using the interface compression technique maintain a constant interface thickness of a few grid cells throughout the computations, whereas the one without compression shows ongoing diffusion. The computed solutions are oscillation free and are in excellent agreement with the exact solution.

6.1.2. Water–air shock–interface interaction

Next we consider a model one-dimensional problem of a water–air interface accelerated by a strong shock in water. Since the acoustic impedance of water is significantly higher than that of air, a strong rarefaction wave is reflected back while a weak shock is transmitted through the air. The incident shock Mach number is 1.8815, which produces a large difference in the reflected rarefaction head and tail speeds: -2.334×10^2 for the head and 2.684×10^{-2} for the tail. This is a challenging test case and conventional shock-capturing methods have been shown to yield inaccurate numerical solutions for similar single-fluid problems involving high density and pressure ratios [51,27]. The initial condition for this problem is

$$\begin{aligned}
 (\rho, u, P) &= \begin{cases} (1.362, 81.25, 2.484 \times 10^4) & \text{for } 0 \leq x \leq 0.2, \\ (1 - 0.999\phi, 0, 1) & \text{for } 0.2 < x \leq 1, \end{cases} \\
 \phi &= \frac{1}{2} \left(1 + \tanh \left(\frac{x - 0.5}{2\epsilon_h} \right) \right), \\
 \gamma &= 1 + \frac{(\gamma_2 - 1)(\gamma_1 - 1)}{\phi(\gamma_1 - 1) + (1 - \phi)(\gamma_2 - 1)}, \\
 P^\infty &= \frac{\gamma - 1}{\gamma} \left(\frac{\gamma_1 P_1^\infty (1 - \phi)}{\gamma_1 - 1} + \frac{\gamma_2 P_2^\infty \phi}{\gamma_2 - 1} \right),
 \end{aligned} \tag{31}$$

where the water is modeled with $\gamma_1 = 4.4$ and $P_1^\infty = 6000$, and the air with $\gamma_2 = 1.4$ and $P_2^\infty = 0$.

Solutions are computed on a uniform grid with and without the interface compression method using 200 and 2000 points as shown in Figs. 6 and 7, respectively. The results are indistinguishable if computed with $CFL = 1.0$, rather than 0.3. Note that without the interface compression method the solution oscillates significantly, with the pressure becoming negative in places. These oscillations persist (not shown) even when a first-order reconstruction is used along with an exact Riemann solver. These unphysical oscillations are especially undesirable because when coupled with a cavitation flow model the numerical computations will predict erroneous formation of vapor phase. On the other hand, simulations utilizing the same flow solver with an interface compression technique remedy this problem and provide a much more accurate solution.

The oscillations in computations without interface compression are most likely linked to the numerical smearing of density and interface function across the contact discontinuity. The error due to cell averaging in a typical shock-capturing finite-volume method can be quite significant in presence of strong rarefaction waves and can easily violate the condition of constancy of pressure and velocity across the contact discontinuity. In order to overcome this problem in single-phase flow computations with strong rarefaction waves, Kudriakov and Hui [27] utilized a contact-strength preserving technique that provides a more accurate estimate of flow variables across the contact discontinuity. In the current two-fluid computations the disparity in the equation of state amplifies the averaging errors. These errors are prominent in simulations without interface compression as growing numerical smearing of the contact discontinuity continues to deteriorate the accuracy of the computed solution.

6.2. Two-dimensional tests

6.2.1. Collapse of an air cavity in water

The first two-dimensional test case is the collapse of an air cavity in water by a Mach 1.72 shock. This problem has been studied extensively [19,37,38,21,31] due to its importance in a wide range of physical and practical phenomena such as sonoluminescence, lithotripsy, and hot-spot formation in explosives. The rectangular computational domain for this problem

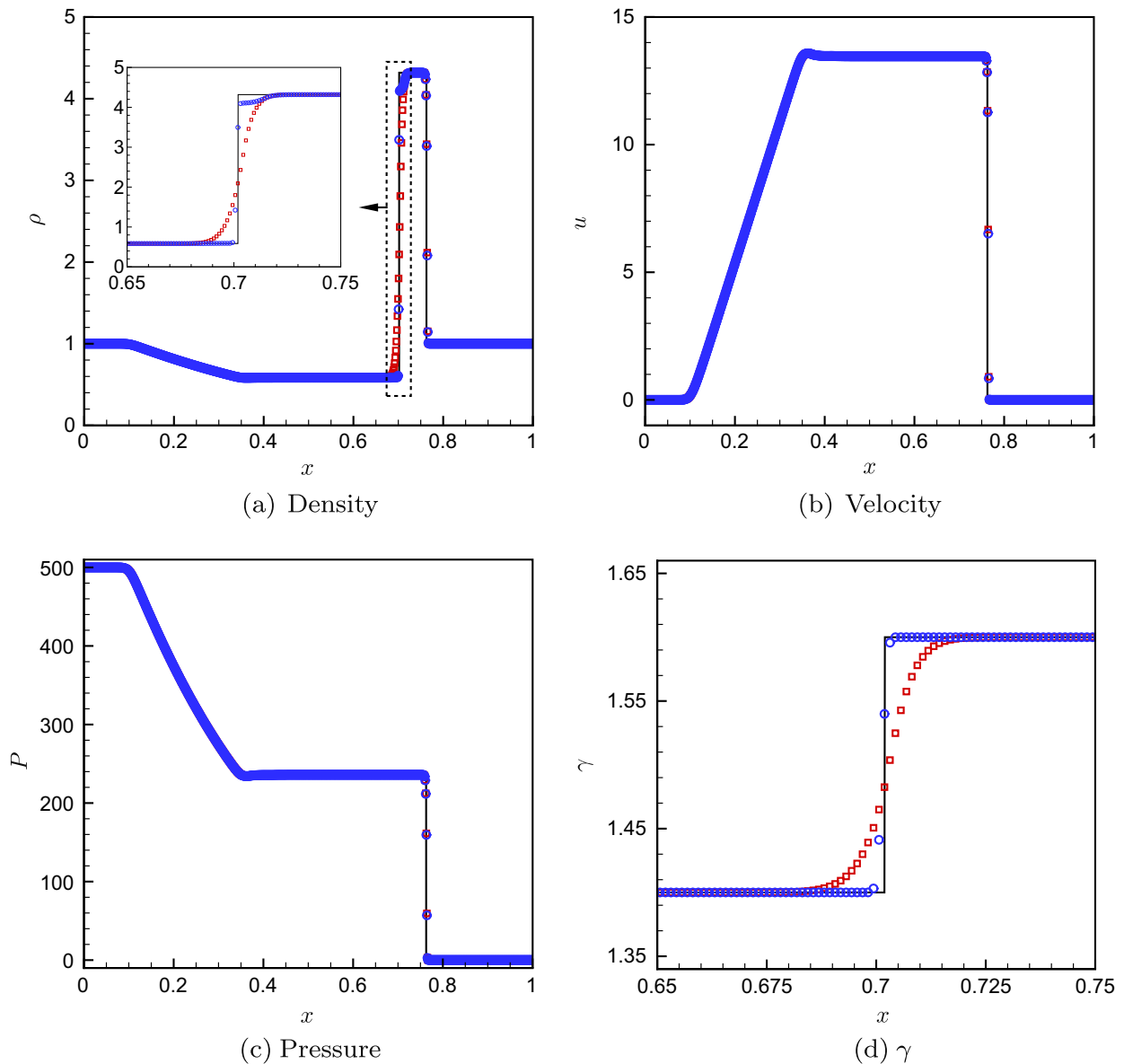


Fig. 5. Solution of the one-dimensional Riemann problem given by (30) computed on a uniform grid with $N = 800$. Solid lines depict the exact solution whereas (○) and (□) denote numerical results computed with and without interface compression, respectively.

is $\Omega = [0, 10] \times [-2.5, 2.5]$. An air bubble of unit radius is placed in water with its center at $(4.375, 0)$, and the shock wave is initiated at $x = 1$ at $t = 0$. The rest of the initial condition is

$$\begin{aligned}
 (\rho, u, v, P) &= \begin{cases} (1.325, 68.52, 0, 1.915 \times 10^4) & \text{if } x \leq 1, \\ (10^{-3} + 0.999\phi, 0, 0, 1), & \text{otherwise,} \end{cases} \\
 \phi &= \frac{1}{2} \left(1 + \tanh \left(\frac{r-1}{2\epsilon_h} \right) \right), \quad r = \sqrt{(x-4.375)^2 + y^2}, \\
 \gamma &= 1 + \frac{(\gamma_2 - 1)(\gamma_1 - 1)}{\phi(\gamma_1 - 1) + (1 - \phi)(\gamma_2 - 1)}, \\
 P^\infty &= \frac{\gamma - 1}{\gamma} \left(\frac{\gamma_1 P_1^\infty (1 - \phi)}{\gamma_1 - 1} + \frac{\gamma_2 P_2^\infty \phi}{\gamma_2 - 1} \right), \tag{32}
 \end{aligned}$$

where $\phi = 0$ in the air and $\phi = 1$ in the water. The equation of state parameters for water and air are set as in the previous examples.

The rectangular computational domain Ω is discretized using a 1600×800 uniform grid. The flow field at various times are shown in Fig. 8. The interface remains thin throughout the simulation even after the cavity fragments due to formation of a high-speed jet. The computed solution shows no spurious oscillations and retains its symmetry about $y = 0$ even though

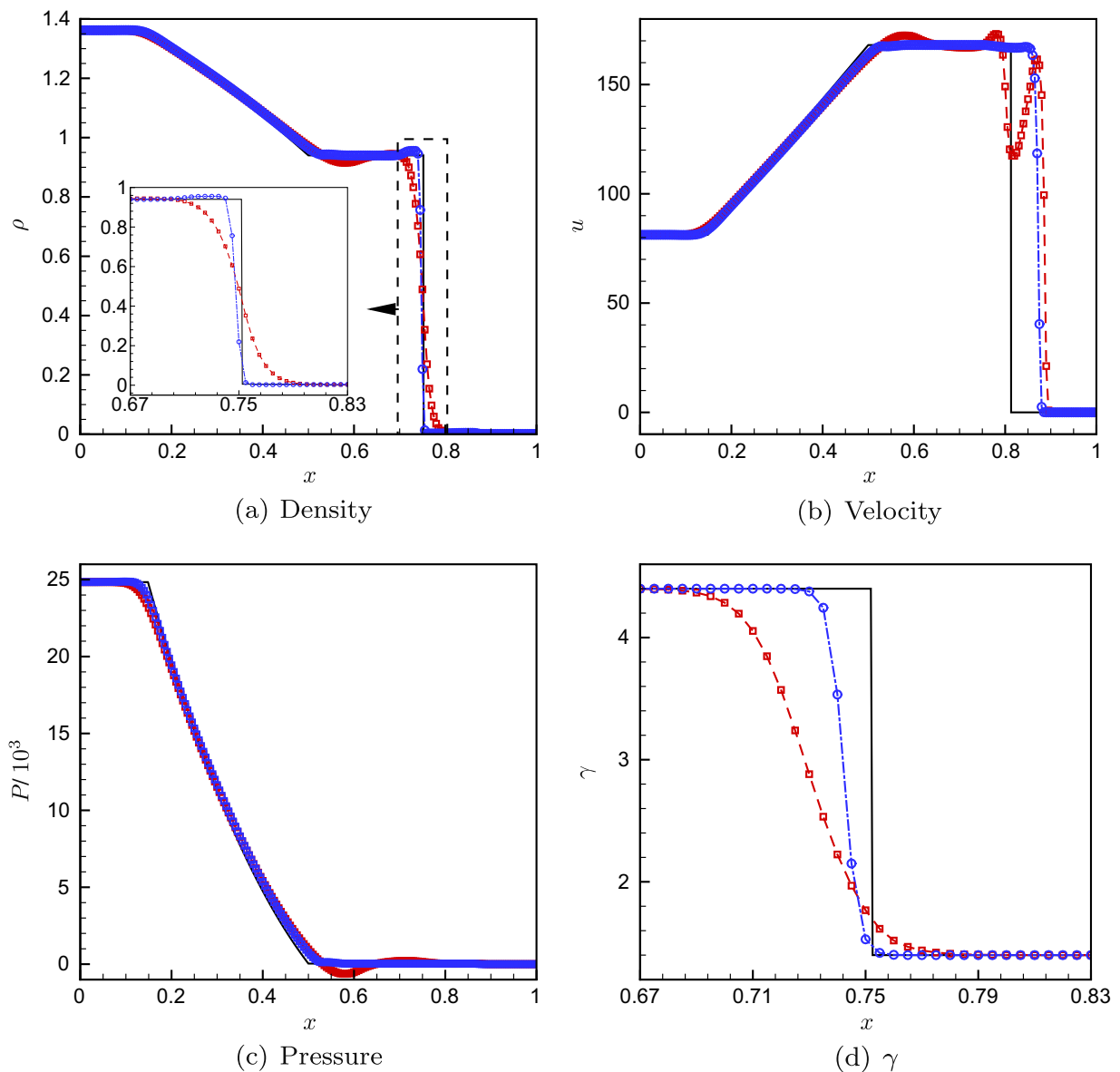


Fig. 6. Solution of the one-dimensional Riemann problem given by (31) computed on a uniform grid with $N = 200$. Solid lines depict the exact solution whereas (\circ) and (\square) denote numerical results computed with and without interface compression, respectively.

no such constraint was enforced in these simulations. The numerical solution is in good agreement with the results of [37], obtained using a flux modification method along with structured adaptive mesh refinement.

Following [39], we assess the convergence of the computed solutions by calculating

$$|\phi|_{\Omega} = \int_{\Omega} \phi \, dx \, dy \approx \sum_{ij} \phi_{ij} \Delta x \Delta y, \tag{33}$$

for simulations utilizing grid resolutions of 400×200 , 600×300 , 800×400 , 1200×600 , 1600×800 and 3200×1600 . We estimate the numerical errors for the first five coarse grids by treating the solution computed on the finest 3200×1600 mesh as the exact reference solution. An estimate of the order of accuracy of the scheme can then be obtained using

$$p = \frac{\log(E_R) - \log(E_C)}{\log(N_C) - \log(N_R)}, \tag{34}$$

where p , E , and N denote order of accuracy, error and number of computational nodes, respectively. Subscripts C and R refer to coarse and refined meshes, respectively. Results are presented in Table 1.

6.2.2. Underwater explosion

In this section we simulate the interaction of a highly compressed cylindrical air bubble placed in water beneath a free surface. This configuration has been considered previously in [33,17,50,37,7] as a model for studying underwater explosions.

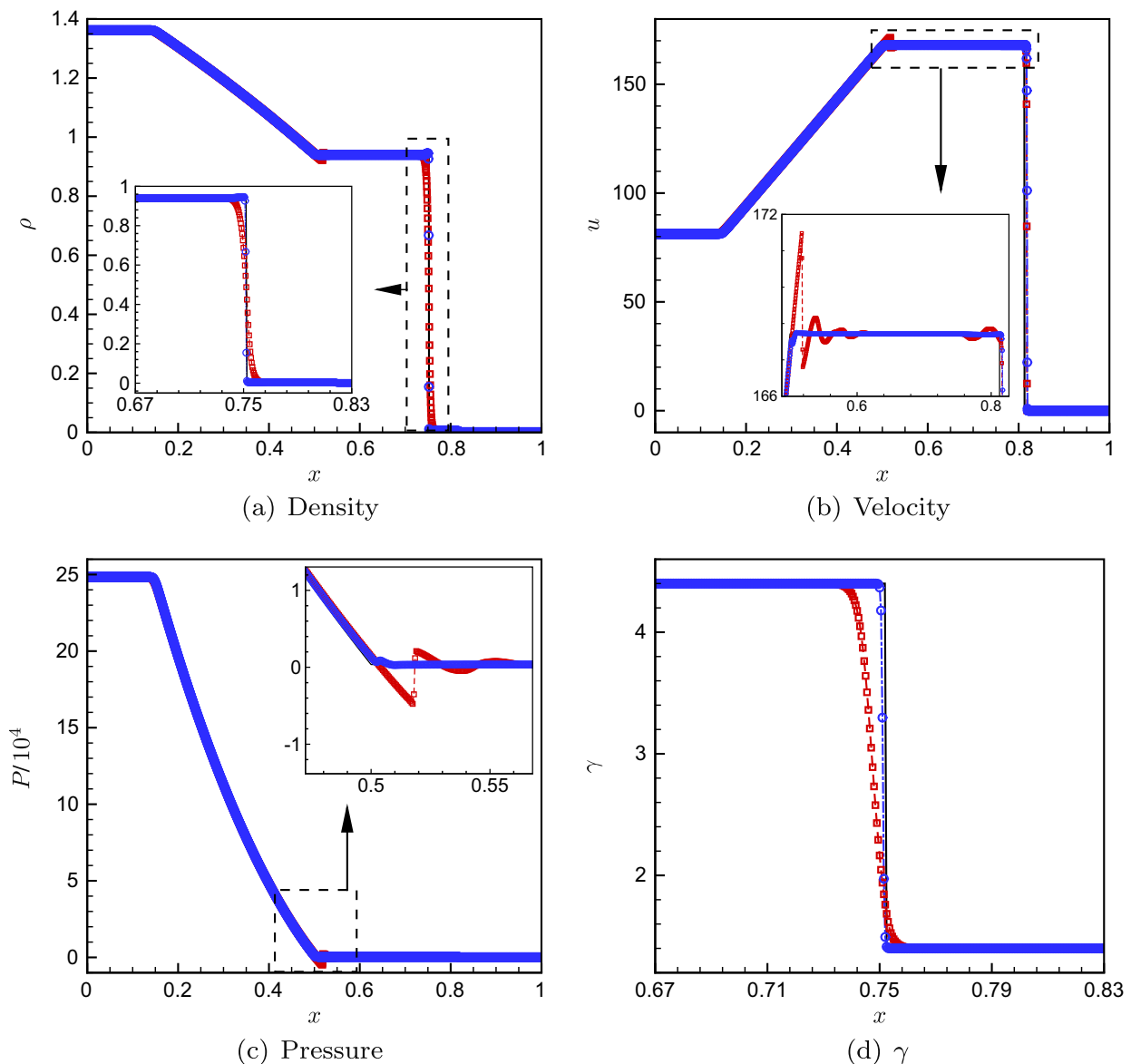


Fig. 7. Solution of the one-dimensional Riemann problem given by (31) computed on a uniform grid with $N = 2000$. Solid lines depict the exact solution whereas (\circ) and (\square) denote numerical results computed with and without interface compression, respectively.

An important challenge of this problem is the topological change in the interface as the bubble bursts through the free surface. The initial condition is

$$\begin{aligned}
 (\rho, u, v, P) &= \begin{cases} (1.225 \times 10^{-3}, 0, 0, 1.01325) & \text{if } y \geq 0, \\ (1.25, 0, 0, 10^4) & \text{if } r \leq 0.12, \\ (1, 0, 0, 1.01325), & \text{otherwise,} \end{cases} \\
 \phi &= \frac{1}{4} \left(1 + \tanh \left(\frac{r - 0.12}{2\epsilon_h} \right) \right) \left(1 - \tanh \left(\frac{y}{2\epsilon_h} \right) \right), \\
 \gamma &= 1 + \frac{(\gamma_2 - 1)(\gamma_1 - 1)}{\phi(\gamma_1 - 1) + (1 - \phi)(\gamma_2 - 1)}, \\
 P^\infty &= \frac{\gamma - 1}{\gamma} \left(\frac{\gamma_1 P_1^\infty (1 - \phi)}{\gamma_1 - 1} + \frac{\gamma_2 P_2^\infty \phi}{\gamma_2 - 1} \right),
 \end{aligned} \tag{35}$$

where $r = \sqrt{x^2 + (y + 0.3)^2}$ and the air and water are modeled as in the previous examples.

Calculations are performed on a computational domain $\Omega = [-2, 2] \times [-1.5, 1.5]$ discretized using a 600×450 uniform grid. Extrapolation boundary conditions are applied on the top ($y = 1.5$) and side ($x = \pm 2$) boundaries of the computational

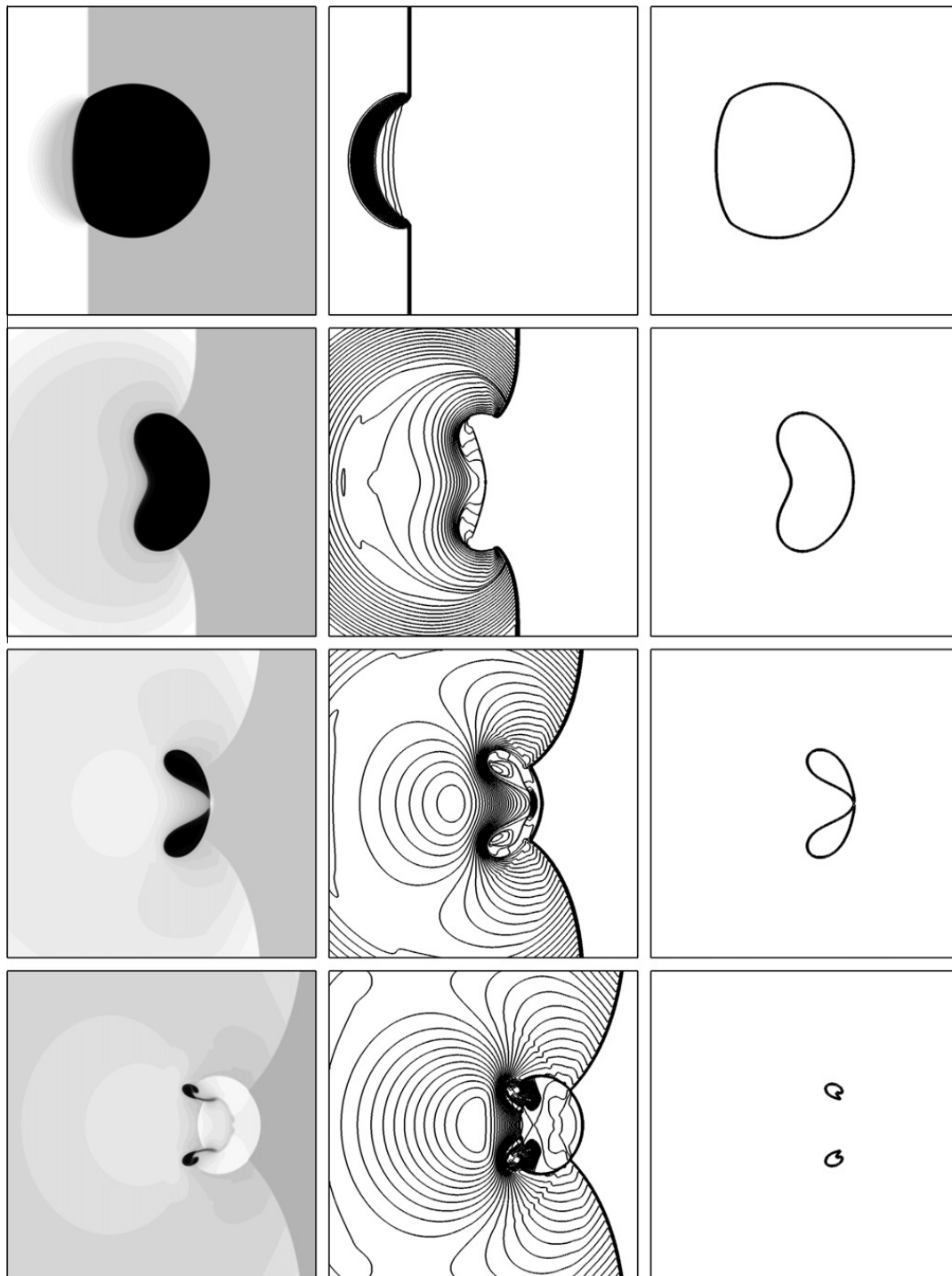


Fig. 8. Density (left), pressure (center) and interface function (right) contours at times $t = 1.0 \times 10^{-2}$, 1.5×10^{-2} , 1.8×10^{-2} , and 2.0×10^{-2} (from top to bottom) for the two-dimensional cavity collapse problem. Contour levels for the interface function range from 0.05 to 0.95.

domain along with reflecting boundary conditions on the bottom edge ($y = -1.5$). Fig. 9 depicts the flow field at different times. In addition to the ϕ and p fields, this flow is also visualized with a numerical schlieren defined as

$$\zeta = \exp\left(-k \frac{|\nabla \rho|}{\max(|\nabla \rho|)}\right), \quad (36)$$

where $k = 100$ if $\phi < 0.5$ and 20 otherwise. It is noted that the computed solutions are free of numerical oscillations and agree well with previously published results. The interface thickness remains constant throughout the simulation both before and after the interfaces merge.

Next we assess the quality of numerical solutions by performing additional calculations using refined grids with 600×450 and 800×600 nodes. The results depicted in Fig. 10 show good agreement between $\phi = 0.5$ isocontour computed

Table 1
Convergence of $|\phi|_{\Omega}$ at various times for different grid resolutions.

Grid	$t = 10^{-2}$			$t = 1.25 \times 10^{-2}$		
	$ \phi _{\Omega}$	Error	p	$ \phi _{\Omega}$	Error	p
400×200	2.91777	2.02×10^{-2}	–	2.19133	2.02×10^{-2}	–
600×300	2.90867	1.11×10^{-2}	1.48	2.18151	1.04×10^{-2}	1.64
800×400	2.90447	6.90×10^{-3}	1.65	2.17747	6.36×10^{-3}	1.71
1200×600	2.90084	3.27×10^{-3}	1.84	2.17419	3.07×10^{-3}	1.79
1600×800	2.89937	1.80×10^{-3}	2.08	2.17287	1.76×10^{-3}	1.94
3200×1600	2.89757	–	–	2.17111	–	–

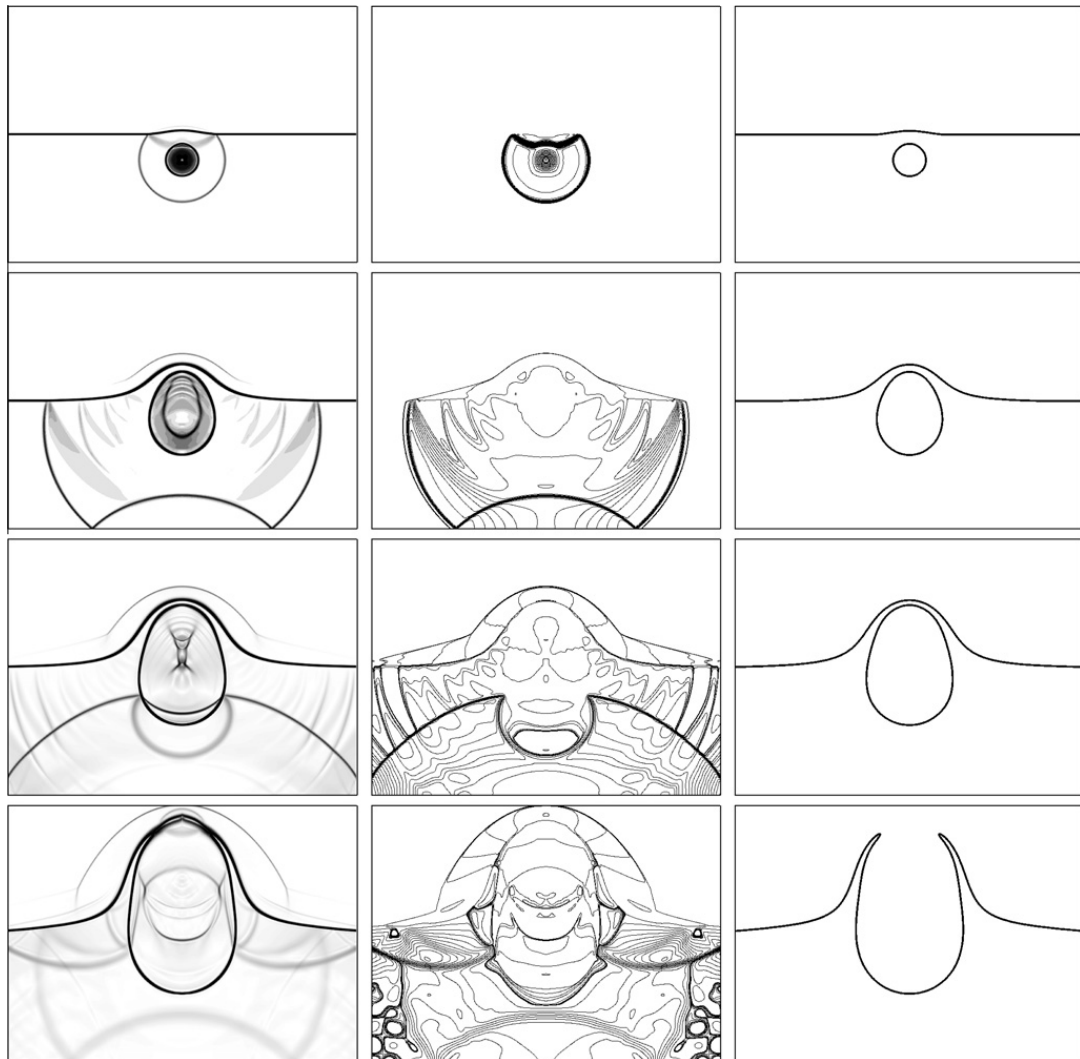


Fig. 9. Numerical schlieren (left), pressure (center) and interface function (right) contours for the underwater explosion problem at times $t = 0.06, 0.25, 0.4$ and 0.5 (from top to bottom). Contour levels for the interface function range from 0.05 to 0.95.

using increasingly refined grids. Of course, as the mesh is refined, there will be times for which the solutions are qualitatively different simply because smaller features can be resolved. Fig. 10 shows such a time. The more resolved solution can support a thinner liquid layer above the bubble. In practice, of course, resolution must be selected based upon the simulation objectives, and in some cases additional physical models must be added, such as the viscosity we have used in a specific application [13].

6.2.3. Mach 6 shock in air hitting a water cylinder

Now we consider the interaction of a Mach 6 shock in air with a cylindrical water column and demonstrate that the numerical methodology developed in the preceding sections is also compatible with high-order formulations utilizing

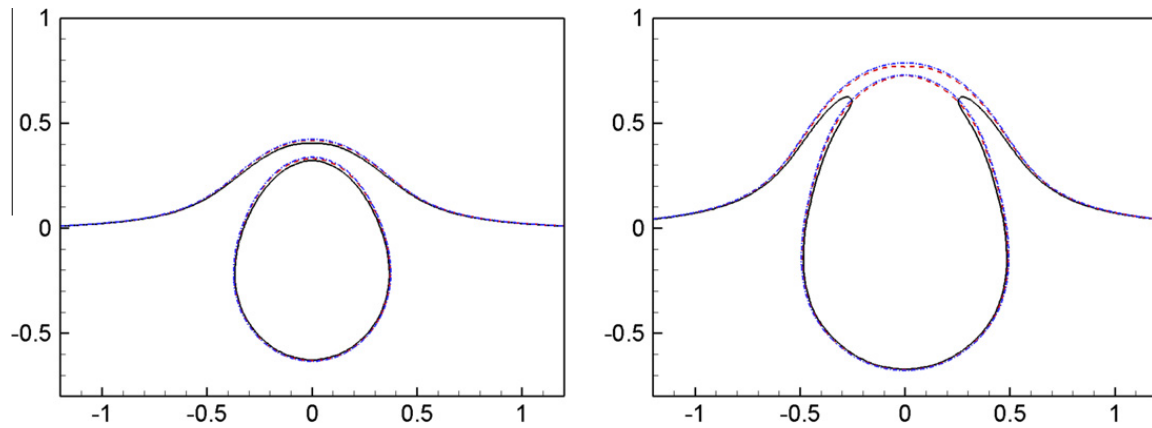


Fig. 10. The 0.5 isopleth of ϕ for the underwater explosion problem at $t = 0.25$ (left) and $t = 0.4$ (right) computed on 400×300 (—), 600×450 (- - -), and 800×600 (- · -) grids.

finite-volume WENO reconstruction [53]. Similar problems have been considered previously [37,7]. The initial condition for this example is

$$\begin{aligned}
 (\rho, u, v, P) &= \begin{cases} (5.268, 5.790, 0, 42.39) & \text{if } x \leq 1, \\ (1 + 999\phi, 0, 0, 1.013), & \text{otherwise,} \end{cases} \\
 \phi &= \frac{1}{2} \left(1 - \tanh \left(\frac{r - 0.562}{2\epsilon_h} \right) \right), \quad r = \sqrt{(x - 2)^2 + y^2}, \\
 \gamma &= 1 + \frac{(\gamma_2 - 1)(\gamma_1 - 1)}{\phi(\gamma_1 - 1) + (1 - \phi)(\gamma_2 - 1)}, \\
 P^\infty &= \frac{\gamma - 1}{\gamma} \left(\frac{\gamma_1 P_1^\infty (1 - \phi)}{\gamma_1 - 1} + \frac{\gamma_2 P_2^\infty \phi}{\gamma_2 - 1} \right),
 \end{aligned} \tag{37}$$

where again air and water are modeled as in the previous examples.

The problem is solved on a rectangular computational domain $\Omega = [0, 8] \times [-1, 1]$ discretized using a 2000×500 uniform grid. Extrapolation boundary conditions are applied on the left ($x = 0$) and right ($x = 8$) boundaries whereas the top ($y = -1$) and bottom ($y = 1$) solid boundaries are modeled using reflecting boundary conditions. Primitive variables (ρ, u, v , and P) are reconstructed [22] using a fifth-order finite-volume WENO scheme developed by Titarev and Toro [53] using Gaussian quadrature nodes in each cell, which yields a fourth-order accurate numerical approximation. Note that the contact discontinuity is captured on the computational grid and its numerical width is determined not by the numerical dissipation of the underlying advection scheme but by the interface compression technique (ϵ_h). It is necessary to use a monotonicity preserving (first-order or TVD) advection scheme so that spurious oscillations are not generated and ϕ remains bounded between 0 and 1. WENO provides more accurate solution in smooth regions of the flow field through high-order reconstruction. However, even a high-order advection scheme based on WENO reconstruction must reduce to first-order close to shocks and contacts in order to remain monotonic. Because the interface function ϕ is constant (0 or 1) away from the discontinuities, there is no benefit of nominally more accurate reconstruction. Therefore, our reconstruction for ϕ would match the effective local order of WENO at discontinuities and away from the interface the convergence of the scheme is immaterial since ϕ is constant there. This does not alter the overall accuracy of the scheme and our shock and contact capturing method is as typical first-order accurate in an L_1 norm.

Fig. 11 depicts the flow field evolution through numerical schlieren and interface function contours. The numerical solution has no obvious oscillations and the interface thickness is confined to a few grid cells throughout the simulation. It is noted that the numerical method successfully captures apparent interfacial instabilities which develop at later times due to baroclinic vorticity deposition at the water–air interface. Results of a grid refinement study performed using 500×125 , 1000×250 and 2000×500 computational nodes are depicted in Fig. 12. We observe good agreement between the $\phi = 0.5$ isocontours computed using increasingly refined grids.

6.3. Three-dimensional tests

6.3.1. Spherically symmetric problem

In order to validate the numerical methodology in multiple dimensions, we simulate a three-dimensional test case for which a spherically symmetric reference solution can be computed. The computational domain for this problem is a cube $\Omega = [-1, 1]^3$, with the initial condition

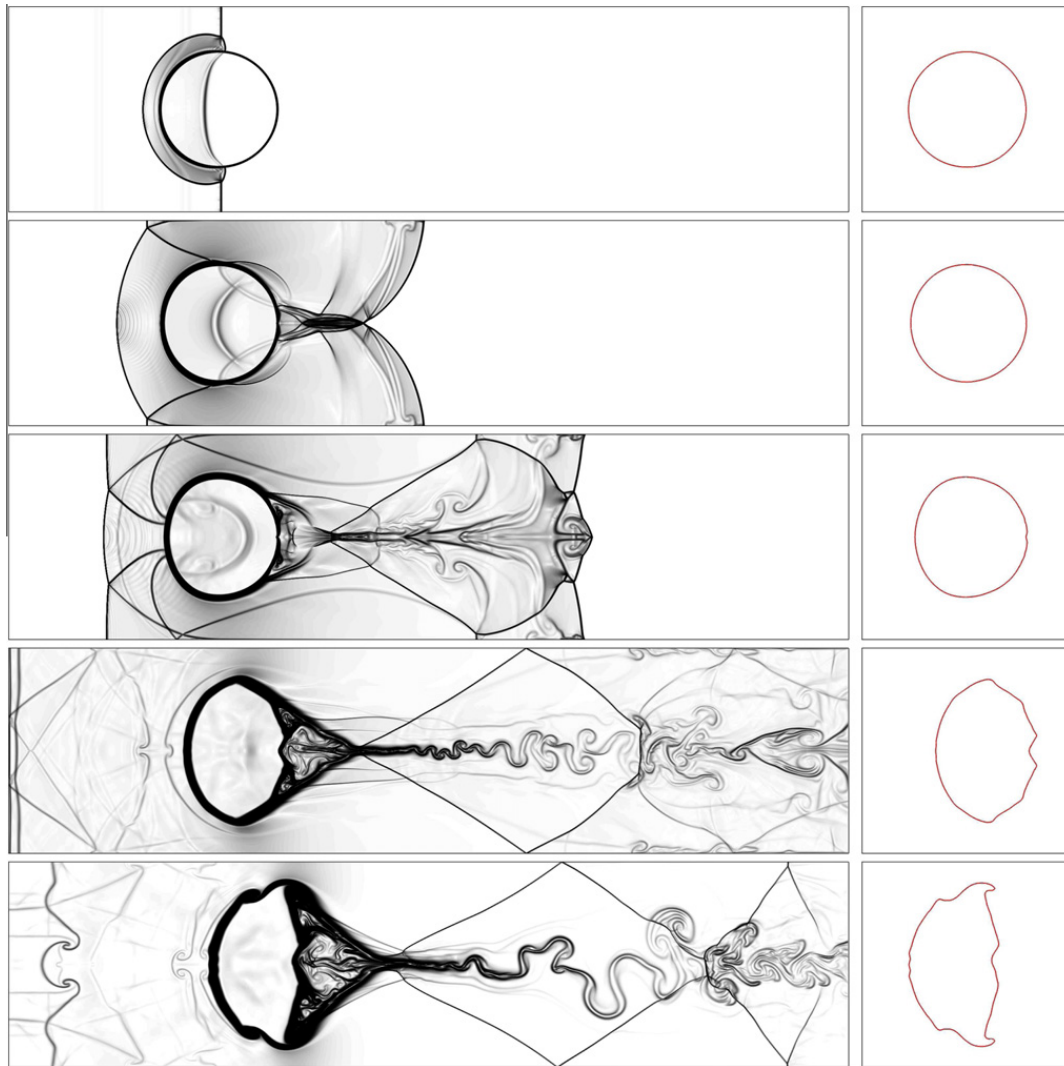


Fig. 11. Numerical schlieren (left) and interface function (right) at time $t = 0.25, 0.5, 0.75, 1.5,$ and 2.15 (from top to bottom) for a Mach 6.0 air–water shock–cylinder interaction problem, computed using a fifth-order WENO scheme on a 2000×500 uniform grid. Contour levels for the interface function range from 0.05 to 0.95.

$$\begin{aligned}
 \rho &= 1.2H_1 + 10^{-3}H_2 + (1 - H_1 - H_2), \\
 \mathbf{u} &= \mathbf{0}, \\
 p &= \begin{cases} 10^4 & \text{if } r \leq 0.25, \\ 1, & \text{otherwise,} \end{cases} \\
 \phi &= H_1 + H_2, \\
 H_1 &= \frac{1}{2} \left(1 - \tanh \left(\frac{r - 0.25}{2\epsilon_h} \right) \right), \\
 H_2 &= \frac{1}{2} \left(1 + \tanh \left(\frac{r - 0.75}{2\epsilon_h} \right) \right), \\
 \gamma &= 1 + \frac{(\gamma_2 - 1)(\gamma_1 - 1)}{\phi(\gamma_1 - 1) + (1 - \phi)(\gamma_2 - 1)}, \\
 p^\infty &= \frac{\gamma - 1}{\gamma} \left(\frac{\gamma_1 P_1^\infty (1 - \phi)}{\gamma_1 - 1} + \frac{\gamma_2 P_2^\infty \phi}{\gamma_2 - 1} \right),
 \end{aligned} \tag{38}$$

where $r = \sqrt{x^2 + y^2 + z^2}$ and the air and water are modeled as before. The simulation uses two sets of uniform computational grids with 121 and 241 cells in each direction. Extrapolation boundary conditions are applied on all six sides of the cubic computational domain. A comparison of the three-dimensional results along the positive x axis with the reference solution, obtained by solving the one-dimensional Euler equation with appropriate geometric source terms on a 10,000-point mesh, is

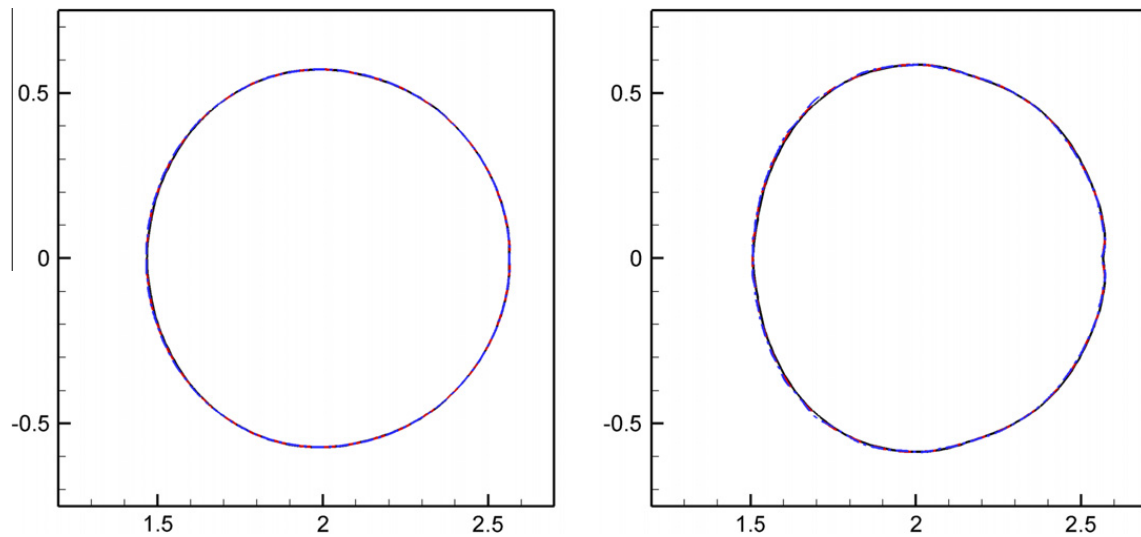


Fig. 12. The 0.5 isopleth of ϕ for the Mach 6.0 air–water shock–cylinder interaction problem at $t = 0.5$ (left) and $t = 0.75$ (right) computed on 500×125 (—), 1000×250 (---), and 2000×500 (-·-·) grids.

depicted in Fig. 13. We observe good agreement between the computed results and the reference solution and the interface is captured accurately in three to four grid cells.

6.3.2. Three-dimensional bubble collapse

The final example is concerned with collapse of two air bubbles in water in the vicinity of a solid wall, attempting to model the phenomena of cavitation damage. A schematic of the problem is shown in Fig. 14. This problem is, in a sense, the most challenging because it tests the robustness of the proposed method for problems involving more than two phases, which are modeled using complicated equations of state in three dimensions. For simplicity, the solid is assumed to be fluid-like so that governing equations for multi-fluid compressible flow still hold. The following Cochran and Chan [10] equation of state for copper is used to model the solid,

$$P = (\gamma_1 - 1)\rho e - ((\gamma - 1)\rho e_0(\rho) - P_0(\rho)),$$

where

$$P_0(\rho) = A_1 \left(\frac{\rho_0}{\rho}\right)^{-E_1} - A_2 \left(\frac{\rho_0}{\rho}\right)^{-E_2},$$

$$e_0(\rho) = -\frac{A_1}{\rho_0(1-E_1)} \left\{ \left(\frac{\rho_0}{\rho}\right)^{1-E_1} - 1 \right\} + \frac{A_2}{\rho_0(1-E_2)} \left\{ \left(\frac{\rho_0}{\rho}\right)^{1-E_2} - 1 \right\} - c_v T_0,$$

were $\gamma_1 = 3$, $c_v = 393$, $A_1 = 1.45667 \times 10^6$, $A_2 = 1.47751 \times 10^6$, $E_1 = 2.994$, $E_2 = 1.994$, $T_0 = 300 \times 10^{-5}$, and $\rho_0 = 8.9$. Real gas effects are accounted for using the following van der Waal's equation of state for the air bubbles

$$P = \frac{\gamma_2 - 1}{1 - b\rho} (\rho e - a\rho^2) - a\rho^2, \tag{39}$$

where $\gamma_1 = 1.4$, $a = 5$, and $b = 1$. The liquid phase is assumed to be sufficiently well described by the stiffened equation of state for water $P = (\gamma_3 - 1)\rho e - \gamma_3 P_3^\infty$, with $\gamma_3 = 4.4$, $P_3^\infty = 6 \times 10^3$. The initial condition is

$$(\rho, u, v, w, P) = \begin{cases} (1.016, 2.541, 0, 0, 405.3) & \text{if } x \leq 0.1, \\ (8.9, 0, 0, 0, 1.013) & \text{if } x \geq 1.25, \\ (10^{-3}, 0, 0, 0, 1.013) & \text{if } r_1 \leq 0.15 \text{ or } r_2 \leq 0.2, \\ (1, 0, 0, 0, 1.013), & \text{otherwise,} \end{cases}$$

$$\phi_g = 1 - \frac{1}{2} \tanh\left(\frac{r_1 - 0.15}{2\epsilon_h}\right) - \frac{1}{2} \tanh\left(\frac{r_2 - 0.2}{2\epsilon_h}\right),$$

$$\phi_s = \frac{1}{2} \left(1 - \tanh\left(\frac{1.25 - x}{2\epsilon_h}\right)\right),$$

$$r_1 = \sqrt{(x - 0.75)^2 + (y - 0.75)^2 + (z - 0.45)^2},$$

$$r_2 = \sqrt{(x - 1)^2 + (y - 0.3)^2 + (z - 0.5)^2},$$

where the interface functions ϕ_s and ϕ_g are unity in solid and gas, respectively, and zero outside.

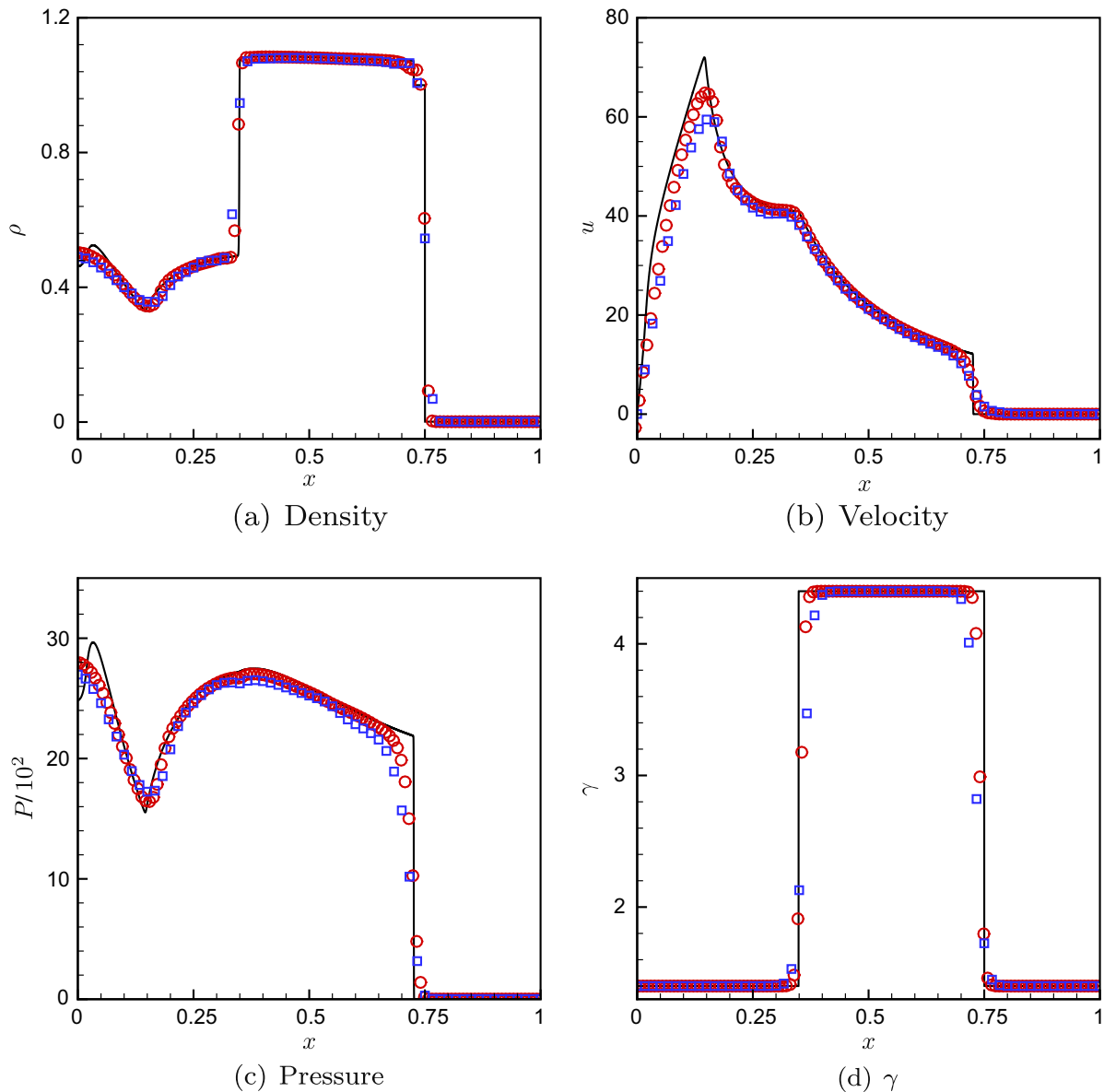


Fig. 13. Solution of the three-dimensional spherically symmetric problem given by (38) computed on a uniform grid with 121 (□) and 241 cells (○) in each direction at $t = 2.5 \times 10^{-3}$. Solid black lines depict the reference solution computed using one-dimensional Euler equations with appropriate geometric source terms.

This problem is simulated on a computational domain $\Omega = [0, 2] \times [0, 1.25] \times [0, 1]$ which is discretized using a $200 \times 125 \times 100$ uniform grid. The flow evolution is depicted in Fig. 15. The incident shock moves in the positive x direction and its interaction with the two air bubbles leads to reflection of strong rarefaction waves (Fig. 15(a) and (b)). At a later time, the incident shock reaches the solid–liquid interface and as shown in Fig. 15(c), a shock is transmitted in the solid (TS) whereas another is reflected back (RS) into the liquid. The volume of the air bubble starts decreasing and reaches a minimum under the effect of high ambient pressure in Fig. 15(d). Subsequent collapse and jetting of the smaller air bubble is accompanied by a spherical blast wave seen in Fig. 15(e). Fig. 15(f)–(h) shows the asymmetric collapse of the larger bubble and its subsequent jetting. The jet eventually reaches the solid wall and causes it to deform as evidenced in the interface function iso-surfaces shown in Fig. 16. In order to access the quality of the computed solutions we perform a convergence study using three different computational grids with $120 \times 75 \times 60$, $160 \times 100 \times 80$ and $200 \times 125 \times 100$ nodes. The computed solution shows reasonably good convergence as evident from the $\phi_g = 0.5$ and $\phi_s = 0.5$ isocontours along $z = 0.5$ midplane at $t = 0.01$ depicted in Fig. 17.

7. Conservation properties

The interface compression techniques raise natural questions regarding their conservation properties, since they rely on modifying the governing equations. Usually, conservation is understood as the ability of the discretization to preserve a

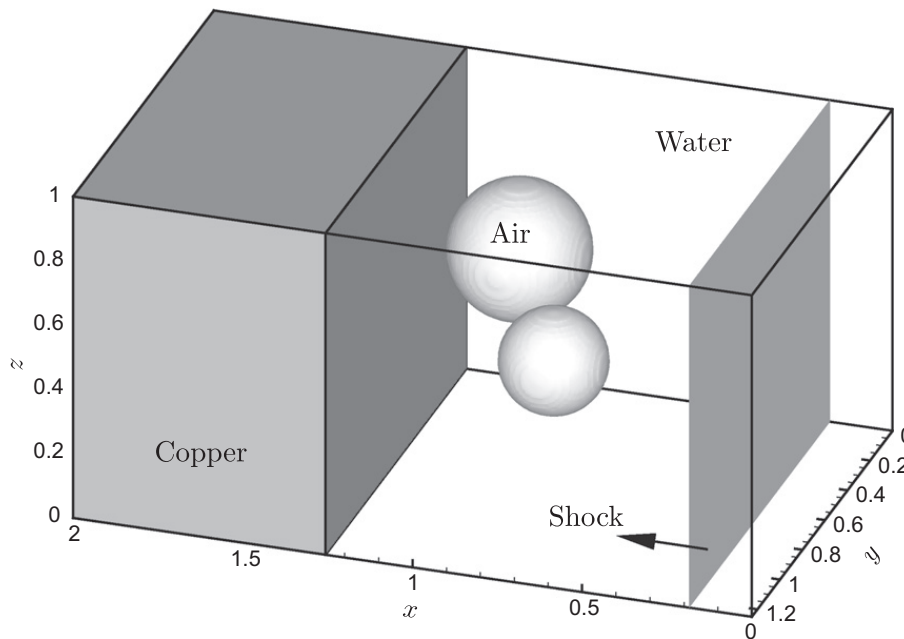


Fig. 14. Schematic for collapse of two air bubbles in water close to a solid wall.

certain invariant, e.g., mass in a closed or periodic domain. In more general terms, conservation of a discretization is a statement regarding the convergence of weak solutions of the conservative form of the transport equations as the mesh is refined [28]. An analysis to establish this behavior of the interface compression methods is presented here.

For simplicity, we consider the one-dimensional form of (7). More general cases will be discussed at the end of this section. The starting point is

$$\frac{\partial q}{\partial t} + \frac{\partial f(q)}{\partial x} = \rho_1(x, t) \mathcal{U}_o \frac{\partial K}{\partial x}, \quad (41)$$

where

$$K = \epsilon_h \frac{\partial \phi}{\partial x} - \phi(1 - \phi), \quad (42)$$

and $q = \rho_1 \phi$ and $f = \rho_1 u \phi$, with the boundary conditions $\phi(x \rightarrow -\infty, t) = 0$ and $\phi(x \rightarrow \infty, t) = 1$. Using an increasing ϕ facilitates removal in (42) of the absolute value in (4). Furthermore, we define the small nondimensional parameter σ , such that

$$\mathcal{U}_o = \frac{\|u\|_\infty}{\sigma}, \quad (43)$$

where $\|u\|_\infty$ denotes the maximum norm in space and time. For $\epsilon_h \rightarrow 0$ and $\sigma \rightarrow 0$, it is possible to formally develop an asymptotic solution of (41) which is uniformly convergent for $\sigma < \sigma_c$, for some constant σ_c possibly dependent on ϵ_h but independent of $\|u\|_\infty$. First, we define a stretched inner variable

$$\eta = \frac{x - x_i(t)}{\epsilon_h}, \quad (44)$$

where the location of the center of the interface with initial position x_o , $\phi(x_o, 0) = 1/2$, is governed by

$$\frac{dx_i}{dt} = u^*(t), \quad (45)$$

where $u^*(t)$ is certainly equal to $u(x_i(t), t)$ when $u(x, t)$ is smooth and it will take a particular value shown below if a shock coincides with $x_i(t)$. We incorporate the ansatz that ϕ varies in a region of thickness ϵ_h around x_i and we will latter verify that this is indeed the case. Furthermore, we assume that ϵ_h and σ are made small simultaneously according to

$$\epsilon_h = \mathcal{L}_o \sigma, \quad (46)$$

where \mathcal{L}_o denotes the smallest physical length-scale in the flow; this ensures that the physical processes are separate from the artificial compression processes. Now that ϵ_h and σ are related, the corresponding inner expansion, valid in a region where $|\eta| = O(1)$, has the form

$$\phi = \phi_o + \sigma \phi_1 + \sigma^2 \phi_2 + \dots, \quad (47)$$

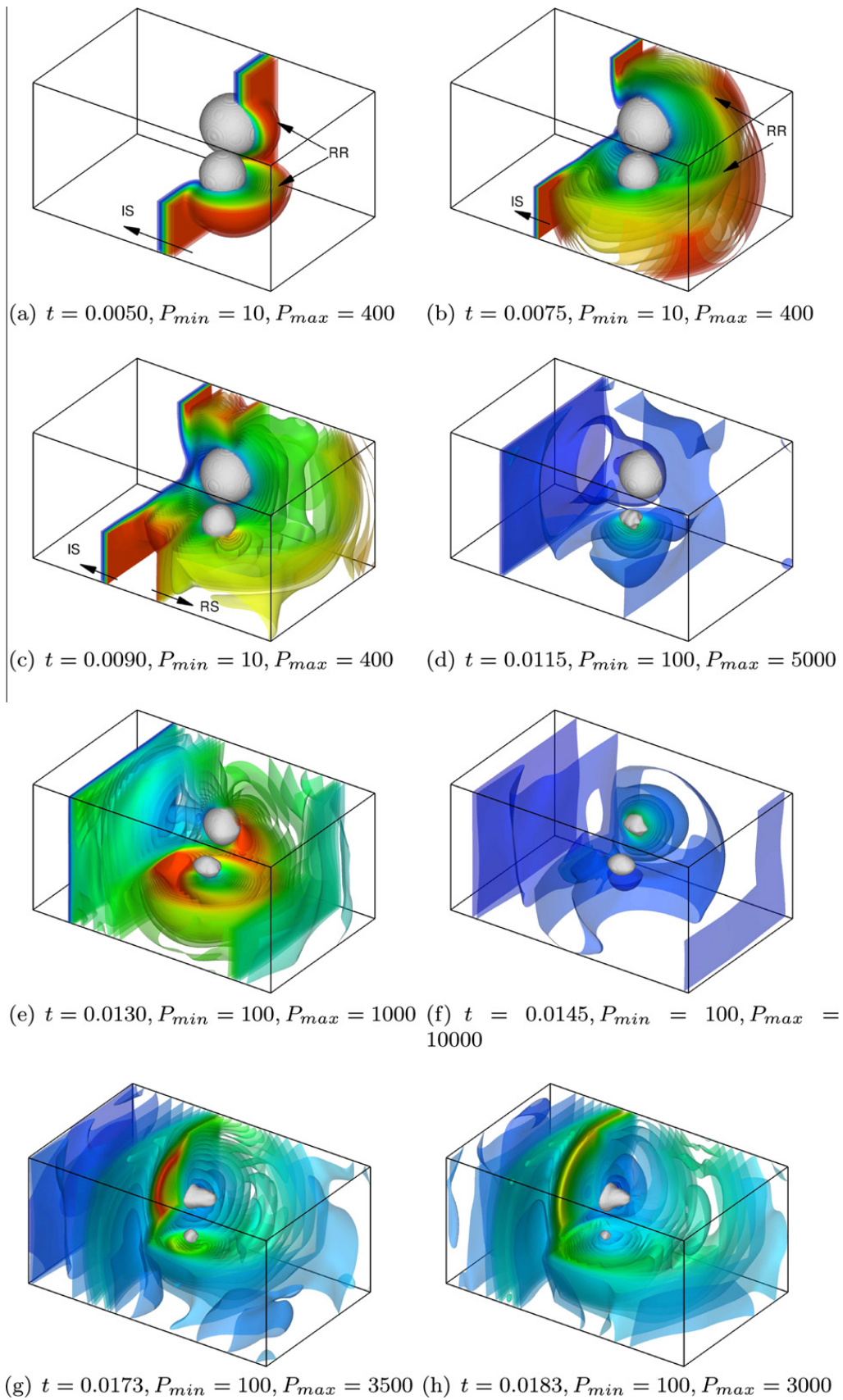


Fig. 15. Pressure iso-surfaces as a function of time for collapse of two air bubbles in water. Each plot shows 30 isocontours between P_{min} and P_{max} with red and blue colors representing maximum and minimum, respectively. Bubbles are depicted as a three-dimensional gray surface. Letters indicate the incident shock (IS), the reflected rarefaction wave (RR), the transmitted shock (TS) and the reflected shock (RS). (For interpretation of the references in colour in this figure legend, the reader is referred to the web version of this article.)

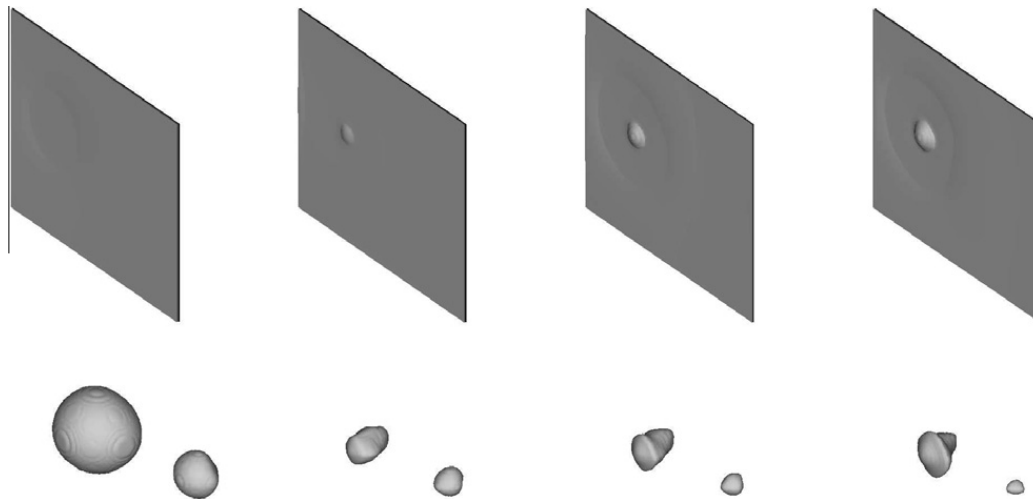


Fig. 16. Three-dimensional surface of interface functions (top) ϕ_s and (bottom) ϕ_g at times $t = 0.0100, 0.0160, 0.0175,$ and 0.0185 (from left to right) for collapse of two air bubbles in water located close to a solid wall.

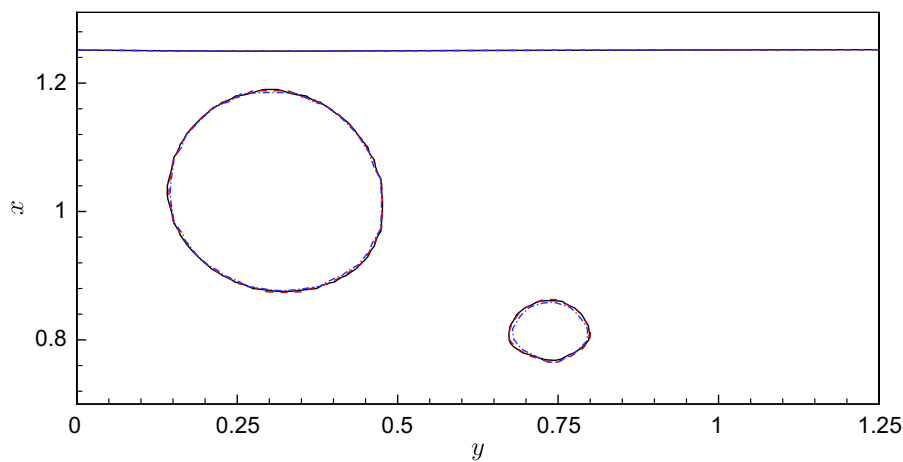


Fig. 17. The 0.5 isopleth of ϕ_g and ϕ_s along $z = 0.5$ plane for the three-dimensional bubble collapse at $t = 0.01$ computed on $200 \times 125 \times 100$ (—), $160 \times 100 \times 80$ (- - -), and $120 \times 75 \times 60$ (- · -) grids.

where $\phi_0, \phi_1, \phi_2, \dots$, are functions to be determined. Introducing these new variables and functions into (41), gives

$$\sigma \left(\epsilon_h \frac{\partial q}{\partial t} + \frac{\partial f}{\partial \eta} - u^*(t) \frac{\partial q}{\partial \eta} \right) = \rho_1 \|u\|_\infty \frac{\partial k}{\partial \eta}, \tag{48}$$

where

$$k = \frac{\partial \phi}{\partial \eta} - \phi(1 - \phi). \tag{49}$$

Expanding k according to

$$k = k_0 + \sigma k_1 + \sigma^2 k_2 + \dots \tag{50}$$

and grouping terms of the same order in σ , gives

$$k_0 = \frac{\partial \phi_0}{\partial \eta} - \phi_0(1 - \phi_0), \tag{51}$$

$$k_1 = \frac{\partial \phi_1}{\partial \eta} - \phi_1(1 - 2\phi_0), \tag{52}$$

$$k_2 = \frac{\partial \phi_2}{\partial \eta} - \phi_2(1 - 2\phi_0) + \phi_1^2, \tag{53}$$

⋮

Since $\rho_1 > 0$, the leading order solution in σ to (48) is

$$\frac{\partial k_o}{\partial \eta} = 0, \tag{54}$$

or, equivalently, k_o constant. The value of this constant can be determined by matching the solution to outer expansions to the left and right of the interface. These outer expansions can be expressed as

$$\Phi = \Phi_o + \sigma \Phi_1 + \sigma^2 \Phi_2 + \dots, \tag{55}$$

where $\Phi_o, \Phi_1, \Phi_2, \dots$, denote two sets of functions at each side of the interface. (Strictly speaking we should denote them by Φ_i^\pm , but it will be shown below that there is no need to complicate the notation since they can be determined easily.) The resulting outer equations are obtained from

$$\sigma \left(\frac{\partial q}{\partial t} + \frac{\partial f}{\partial x} \right) = \rho_1 \|u\|_\infty \frac{\partial K}{\partial x}, \tag{56}$$

where

$$K = \epsilon_h \frac{\partial \Phi}{\partial x} - \Phi(1 - \Phi). \tag{57}$$

Expanding K according to

$$K = K_o + \sigma K_1 + \sigma^2 K_2 + \dots, \tag{58}$$

and identifying terms gives

$$K_o = -\Phi_o(1 - \Phi_o), \tag{59}$$

$$K_1 = \mathcal{L}_o \frac{\partial \Phi_o}{\partial x} - \Phi_1(1 - 2\Phi_o), \tag{60}$$

$$K_2 = \mathcal{L}_o \frac{\partial \Phi_1}{\partial x} - \Phi_2(1 - 2\Phi_o) + \Phi_1^2, \tag{61}$$

⋮

Then, to leading order, the solution of (56) is

$$\frac{\partial K_o}{\partial x} = 0. \tag{62}$$

Upon using the boundary conditions, it is clear that $\Phi_o = 0$ or 1 on each side of the interface, so $K_o = 0$, which is also valid on both sides of the interface. Matching inner and outer solutions gives (3), to leading order. This solution can be written in inner coordinates as

$$\phi_o = \frac{1}{2} \left(1 + \tanh \left(\frac{\eta}{2} \right) \right). \tag{63}$$

One can carry out the analysis of the higher-order outer expansion terms in (55) and observe that due to the linearity of q and f on ϕ , all functions are equal to zero, i.e., $\Phi_i = 0$ for $i > 0$, to any algebraic order in σ . This is the key result since it implies that the variation of ϕ is confined to a narrow band of thickness $O(\epsilon_h)$. The fact that the $\Phi_i = 0$ for $i > 0$ can be determined independently of the ϕ_i simplifies the analysis greatly, but it does not imply that ϕ_i are zero for $i > 0$. In fact, ϕ_1 is determined from

$$\frac{\partial f_o}{\partial \eta} - u^*(t) \frac{\partial q_o}{\partial \eta} = \rho_1 \|u\|_\infty \frac{\partial k_1}{\partial \eta}, \tag{64}$$

where q_o and f_o denote q and f evaluated at ϕ_o . The boundary conditions, determined by matching with the outer solution determined previously, are $\phi_1 = 0$ at $\eta \rightarrow \pm\infty$. In some circumstances, e.g., when $u(x,t) \sim u(x_i(t),t) + O(\epsilon_h)$ and $\rho_1(x,t) \sim \rho_1(x_i(t),t) + O(\epsilon_h)$, (64) gives $\phi_1 \equiv 0$. This can be verified by expanding the expression for $q_o = \rho_1 \phi_o$ and $f_o = \rho_1 u \phi_o$ about $x = x_i(t)$. Otherwise, e.g., during a shock interaction where the velocity is not smooth but f is continuous, there may be a non-zero function ϕ_1 that could, in principle, satisfy (64) with $\phi_1 \neq 0$. Eq. (64) can be formally integrated if we define the function $g(\eta,t)$ via

$$g(\eta,t) = \frac{1}{\rho_1 \|u\|_\infty} \left(\frac{\partial f_o}{\partial \eta} - u^*(t) \frac{\partial q_o}{\partial \eta} \right). \tag{65}$$

Time appears only parametrically in (64) and therefore requires no further consideration. Then, the exact integral of (64) is given by

$$\phi_1 = \frac{c_1 + \int_0^\eta \cosh^2(\eta'/2) \left(\int_0^{\eta'} g(\eta'', t) d\eta'' \right) d\eta'}{\cosh^2(\eta/2)}. \tag{66}$$

The integrals in (66) converge because g goes to zero quickly as $|\eta| \rightarrow \infty$ due to ϕ_o . The only unresolved issue with (66) is that one cannot determine c_1 from the boundary conditions, $\phi_1 \rightarrow 0$ as $|\eta| \rightarrow \infty$ (this is related to the appearance of exponentially small terms $\sim \cosh^{-2}(\eta/2)$). The constant c_1 can be obtained by enforcing that $\phi(0, t) = 1/2$, which implies $\phi_1(0, t) = 0$ and $c_1 = 0$ (since $\phi_o(0, t) = 1/2$). The analysis presented above for ϕ_1 carries over, with minor modifications, to the higher-order terms of the inner expansion since these equations are linear.

After these, rather lengthy, preliminaries we can address the issue of conservation. We follow the general approach (e.g. [26], see Section 4.4, pp. 141–156), and seek weak solutions of (41) by multiplication with a smooth (C^∞) test function of compact support, $\varphi(x, t)$. Integrating by parts the weak solutions obey

$$- \int_0^T \int_{-\infty}^{\infty} q \varphi_t + f \varphi_x dx dt + \int_{-\infty}^{\infty} q(x, 0) \varphi(x, 0) dx = \frac{1}{\sigma} \int_0^{\infty} \int_{-\infty}^{\infty} \varphi \rho_1 \|u\|_\infty \frac{\partial K}{\partial x} dx dt. \tag{67}$$

The issue at hand is whether the term in the right-hand side of (67) approaches zero as $\sigma \rightarrow 0$. This is the general statement of conservation, which implies among other things that the Rankine–Hugoniot relationships will be satisfied at discontinuities and, therefore, waves propagate at the correct speeds. We presume that the discretization of the term in the left-hand side will be conservative and so is of not further concern. As we have seen previously, K can be decomposed as an asymptotic expansion in the small parameter σ . Moreover, one can evaluate the integral in the right-hand side of (67) directly using inner coordinates since the outer expansion is identically zero. Therefore, to leading order, the right-hand side of (67) can be reduced, using (64), to

$$\begin{aligned} & \frac{1}{\sigma} \int_0^{\infty} \int_{-\infty}^{\infty} \varphi(x_i, t) \rho_1 \|u\|_\infty \left(\frac{\partial k_0}{\partial \eta} + \sigma \frac{\partial k_1}{\partial \eta} + \dots \right) d\eta dt + O(\epsilon_h) = \int_0^{\infty} \int_{-\infty}^{\infty} \varphi(x_i, t) \rho_1 \|u\|_\infty \frac{\partial k_1}{\partial \eta} d\eta dt + O(\epsilon_h) \\ & = \int_0^{\infty} \int_{-\infty}^{\infty} \varphi(x_i, t) \left(\frac{\partial f_o}{\partial \eta} - u^*(t) \frac{\partial q_o}{\partial \eta} \right) d\eta dt + O(\epsilon_h) = \int_0^{\infty} \varphi(x_i, t) [f_o - u^*(t) q_o]_{-\infty}^{\infty} dt + O(\epsilon_h) \sim O(\epsilon_h), \end{aligned} \tag{68}$$

if $u^*(t)$ is defined according to

$$u^*(t) = \begin{cases} u(x_i(t), t) & \text{if } u(x, t) \text{ is smooth at } x = x_i(t), \\ \frac{[f_o]}{[q_o]}, & \text{otherwise,} \end{cases} \tag{69}$$

where $[]$ denotes the jump in q_o and f_o across the interface, $x \rightarrow x_i^\pm$. Obviously, (69) is a result of the correct Rankine–Hugoniot relationship and u^* is the appropriate speed of the interface. The term $O(\epsilon_h)$ in (68) arises when $\varphi(x, t)$ is expanded around $x = x_i(t) + \epsilon_h \eta$. In consequence, (67) has the form

$$- \int_0^T \int_{-\infty}^{\infty} q \varphi_t + f \varphi_x dx dt + \int_{-\infty}^{\infty} q(x, 0) \varphi(x, 0) dx = \sigma \int_0^{\infty} \int_{-\infty}^{\infty} \varphi F(\rho_1, \phi, u) dx dt + O(\sigma^2), \tag{70}$$

where we have taken into account that $\epsilon_h = O(\sigma)$ and F denotes a function of order unity incorporating the left-over terms of the asymptotic expansion. In particular, if the numerical implementation of the left-hand side of (41) is conservative according to [28], the new interface compression will be conservative as well in the limit as $\sigma \rightarrow 0$, since the right-hand side of (70) goes to zero. This converges to the weak form of (7), with zero right-hand side, when $\sigma \rightarrow 0$. In practice, one is forced to take $\epsilon_h \sim h$, where h is the numerical grid spacing, in order for the compression terms to be numerically resolved. Therefore, the method becomes conservative, in the generalized sense, when $h \rightarrow 0$, as proved by [28] for the advection part of the equation.

The generalization to two and three dimensions are straightforward, albeit cumbersome, if the compression term is of the new form (5), because $\mathbf{n} \cdot \nabla = \partial/\partial n$. This immediately allows a local change of variables into normal and tangential coordinates. The asymptotic analysis in the normal direction is analogous to that presented above for the one-dimensional case. If the compression term is in divergence form, (2), there is an additional curvature term, see (6), which may complicate the analysis.

8. Conclusions

An interface compression technique is presented in order to counter the diffusion of multi-fluid interfaces in compressible flows caused by numerical dissipation. A new interface function method is developed in order to overcome the deficiencies of the original conservative level-set method. A monotonicity preserving density correction technique is developed in order to ensure the consistency of the numerical solution. The conservation properties of the compression technique, introduced in the methodology to keep the interface sharp, are shown to converge to the ideal solution with increasing grid resolution. The PDE based method does not require a priori knowledge of the location of the interface and naturally handles topological changes including merging and fragmentation. Several numerical examples confirm the utility, accuracy and convergence of the method. The methodology is not tied to a particular shock-capturing method and simulations are presented using an HLLC solver and high-order finite-volume WENO reconstruction. The versatility of the proposed technique in simulating

flows involving more than two phases is demonstrated on a model three-dimensional simulation of the interaction between collapsing bubbles and an adjacent solid wall.

Acknowledgements

This work was supported by the US Department of Energy via the Center for Simulation of Advanced Rockets at the University of Illinois at Urbana-Champaign and AFOSR.

Appendix A. Nonlinear mapping error analysis

This appendix develops a truncation error bound that explicitly demonstrates the benefits of using the nonlinear mapping (9) and the approach introduced in Section 2.3 for the numerical calculation of the interface normals needed by the interface compression scheme. We will discuss the two-dimensional case since the three-dimensional case is analogous but requires slightly more cumbersome algebraic expressions.

We start with a solution for the phase field

$$\phi = \frac{1}{2} \left[1 + \tanh \left(\frac{n}{2\epsilon_h} \right) \right], \tag{A.1}$$

and its mapped field

$$\psi = \frac{\phi^\alpha}{\phi^\alpha + (1 - \phi)^\alpha}, \tag{A.2}$$

which is monotonic for $\alpha < 1$. The coordinate n is measured with respect to the $\phi = 0.5$ isopleth of (A.1), given by the curve

$$\mathbf{x} = \mathbf{X}(s), \tag{A.3}$$

where $s \in [0, L]$ denotes the arc-length and L is the curve length. The usual geometry relations indicate that

$$\mathbf{n} = (\mathbf{x} - \mathbf{X}(s)) \cdot \mathbf{n}, \tag{A.4}$$

together with

$$(\mathbf{x} - \mathbf{X}(s)) \cdot \mathbf{t} = 0, \tag{A.5}$$

where \mathbf{n} and \mathbf{t} denote the normal and tangent vectors, respectively, at the closest point of the curve, s . Note that (A.5) has at least one solution for an open (periodic) curve and two or more solutions for a closed curve. For this analysis we assume that the resolution is sufficient so that only the closest solution is relevant. The vectors \mathbf{n} and \mathbf{t} are given by

$$\mathbf{t} = \frac{d\mathbf{X}}{ds} = \begin{bmatrix} -\sin(\theta) \\ \cos(\theta) \end{bmatrix}, \quad \mathbf{n} = \begin{bmatrix} \cos(\theta) \\ \sin(\theta) \end{bmatrix}, \tag{A.6}$$

where

$$\sin(\theta) = -\frac{dX}{ds}, \quad \cos(\theta) = \frac{dY}{ds}. \tag{A.7}$$

The dependence of the error in the calculation of the normal as a function of α is developed from the truncation errors of the finite-difference operators used to evaluate \mathbf{n} . The accuracy of a centered first-derivative approximation in grid direction x , with spacing Δx , is proportional to the leading order term of the Taylor expansion according to

$$D_x \phi = \frac{\partial \phi}{\partial x} + \frac{1}{(p+1)!} \frac{d^{p+1} \phi}{dx^{p+1}} \Delta x^p + O(\Delta x^{p+1}), \tag{A.8}$$

where p is the order of accuracy of the approximation. Retaining the leading order terms, the truncation error of the discretely calculated normal at any point is given by

$$T^p[\phi] = \frac{1}{(p+1)! |\nabla \phi|} \begin{bmatrix} \frac{d^{p+1} \phi}{dx^{p+1}} \Delta x^p - \frac{1}{|\nabla \phi|^2} \frac{\partial \phi}{\partial x} \left(\frac{d^{p+1} \phi}{dx^{p+1}} \Delta x^p \frac{\partial \phi}{\partial x} + \frac{d^{p+1} \phi}{dy^{p+1}} \Delta y^p \frac{\partial \phi}{\partial y} \right) \\ \frac{d^{p+1} \phi}{dy^{p+1}} \Delta y^p - \frac{1}{|\nabla \phi|^2} \frac{\partial \phi}{\partial y} \left(\frac{d^{p+1} \phi}{dx^{p+1}} \Delta x^p \frac{\partial \phi}{\partial x} + \frac{d^{p+1} \phi}{dy^{p+1}} \Delta y^p \frac{\partial \phi}{\partial y} \right) \end{bmatrix}. \tag{A.9}$$

This discretization error needs to be compared with $T^p[\psi]$ to assess the computational advantage of the mapping. For simplicity, we assume that $\Delta x = \Delta y = \Delta$ and consider the case $p = 2$. For the change of variables (A.2) the following relationships are needed

$$\psi = f(\phi), \tag{A.10}$$

$$\delta\psi = f'\delta\phi, \tag{A.11}$$

$$\delta^2\psi = f''(\delta\phi)^2 + f'\delta^2\phi, \tag{A.12}$$

$$\delta^3\psi = f'''(\delta\phi)^3 + 3f''\delta\phi\delta^2\phi + f'\delta^3\phi, \tag{A.13}$$

where $f(\phi)$ is given by (A.2) and δ denotes the differential (infinitesimal difference) operator. Then

$$T^2[\psi] = \frac{\Delta^2}{3!|\nabla\phi|} \left[\frac{f'''}{f'} \left(\frac{d\phi}{dx} \right)^3 + 3\frac{f''}{f'} \frac{d\phi}{dx} \frac{d^2\phi}{dx^2} + \frac{d^3\phi}{dx^3} - A \frac{\partial\phi}{\partial x} \right], \tag{A.14}$$

where

$$A = \frac{1}{|\nabla\phi|^2} \left[\frac{f'''}{f'} \left(\left[\frac{d\phi}{dx} \right]^4 + \left[\frac{d\phi}{dy} \right]^4 \right) + 3\frac{f''}{f'} \left(\left[\frac{d\phi}{dx} \right]^2 \frac{d^2\phi}{dx^2} + \left[\frac{d\phi}{dy} \right]^2 \frac{d^2\phi}{dy^2} \right) + \frac{d^3\phi}{dx^3} \frac{\partial\phi}{\partial x} + \frac{d^3\phi}{dy^3} \frac{\partial\phi}{\partial y} \right]. \tag{A.15}$$

The derivatives of ϕ with respect to x (and y) are then obtained using (A.1) and the geometrical relationships (A.4) and (A.5), whose derivatives are given by

$$\frac{\partial n}{\partial x} = n_x - \mathbf{t} \cdot \mathbf{n} \frac{\partial s}{\partial x} + \mathbf{nn} \cdot \frac{\partial \mathbf{n}}{\partial x} = n_x + \frac{n}{2} \frac{\partial(\mathbf{n} \cdot \mathbf{n})}{\partial x} = n_x, \tag{A.16}$$

and

$$t_x - \mathbf{t} \cdot \mathbf{t} \frac{\partial s}{\partial x} + \mathbf{nn} \cdot \frac{\partial \mathbf{t}}{\partial x} = t_x - \frac{\partial s}{\partial x} + \mathbf{nn} \cdot \frac{\partial \mathbf{t}}{\partial x} = 0, \tag{A.17}$$

where we have used (A.6) and $(\mathbf{x} - \mathbf{X}) = \mathbf{nn}$, $\mathbf{n} \cdot \mathbf{t} = 0$ and $\mathbf{n} \cdot \mathbf{n} = \mathbf{t} \cdot \mathbf{t} = 1$. The elementary geometrical relationship

$$\frac{\partial \mathbf{t}}{\partial s} = \text{differential}(\cdot)\kappa\mathbf{n}, \tag{A.18}$$

where κ denotes the curvature, can be used to simplify (A.17):

$$\frac{\partial s}{\partial x} = \frac{t_x}{1 - n\kappa}. \tag{A.19}$$

The second- and third-order derivatives are obtained similarly:

$$\frac{\partial^2 n}{\partial x^2} = \frac{\partial n_x}{\partial x} = \frac{\partial n_x}{\partial s} \frac{\partial s}{\partial x} = \frac{n'_x t_x}{1 - n\kappa}, \tag{A.20}$$

$$\frac{\partial^3 n}{\partial x^3} = \frac{t_x}{(1 - n\kappa)^2} \left[(n'_x t_x)' + n'_x \left(n_x \kappa + \frac{nt_x \kappa'}{1 - n\kappa} \right) \right]. \tag{A.21}$$

Analogously to (A.10)–(A.13), the derivatives of ϕ with respect to x (and y) can be obtained through the intermediate n , as follows:

$$\frac{\partial\phi}{\partial x} = \frac{\partial\phi}{\partial n} \frac{\partial n}{\partial x} = \frac{n_x}{4\epsilon_h} \text{sech}^2(\tilde{n}), \tag{A.22}$$

$$\frac{\partial^2\phi}{\partial x^2} = \frac{\partial^2\phi}{\partial n^2} \left(\frac{\partial n}{\partial x} \right)^2 + \frac{\partial\phi}{\partial n} \frac{\partial^2 n}{\partial x^2} = \frac{\text{sech}^2(\tilde{n})}{4\epsilon_h^2} (\beta_x - n_x^2 \tanh(\tilde{n})), \tag{A.23}$$

$$\frac{\partial^3\phi}{\partial x^3} = \frac{\partial^3\phi}{\partial n^3} \left(\frac{\partial n}{\partial x} \right)^3 + 3\frac{\partial^2\phi}{\partial n^2} \frac{\partial n}{\partial x} \frac{\partial^2 n}{\partial x^2} + \frac{\partial\phi}{\partial n} \frac{\partial^3 n}{\partial x^3} = \frac{\text{sech}^2(\tilde{n})}{4\epsilon_h^3} \times \left[\left(\tanh^2(\tilde{n}) - \frac{1}{2} \text{sech}^2(\tilde{n}) \right) n_x^3 - 3n_x \beta_x \tanh(\tilde{n}) + \gamma_x \right], \tag{A.24}$$

where $\tilde{n} = n/(2\epsilon_h)$ and

$$\beta_x = \frac{n'_x t_x \epsilon_h}{1 - n\kappa}, \tag{A.25}$$

$$\gamma_x = \frac{t_x \epsilon_h^2}{(1 - n\kappa)^2} \left[(n'_x t_x)' + n'_x \left(n_x \kappa + \frac{nt_x \kappa'}{1 - n\kappa} \right) \right], \tag{A.26}$$

denote grid-size normalized curvature-related terms. Similar identities are obtained for derivatives in the y direction by suitably replacing x by y . Introducing (A.22)–(A.24) into (A.14) and (A.15) gives, after considerable algebraic manipulations, a transcendental function whose maximum absolute value is reached as $n \rightarrow \pm\infty$, as expected. The limit value is given by

$$T^2[\psi] \rightarrow \frac{\Delta^2}{12\epsilon_h^2} \eta \begin{bmatrix} \sin(\theta) \\ -\cos(\theta) \end{bmatrix}, \quad (\text{A.27})$$

where

$$\eta = 2(\gamma_x \sin(\theta) - \gamma_y \cos(\theta)) + 3\alpha(\beta_y - \beta_x) \sin(2\theta) + \alpha^2 \cos(2\theta) \sin(2\theta). \quad (\text{A.28})$$

The leading order truncation error is thus bounded by

$$|T^2[\psi]| < \frac{\Delta^2}{12\epsilon_h^2} \max_{\theta, \beta_x, \beta_y, \gamma_x, \gamma_y} |\eta|. \quad (\text{A.29})$$

In the current application, $\epsilon_h \sim \Delta$ so the truncation error is controlled by η . Furthermore, note that for the simplest case of a planar interface $\beta_x = \beta_y = \gamma_x = \gamma_y = 0$, without a mapping ($\alpha = 1$) the truncation error is of the same order of magnitude as the approximation. It is not surprising then that one encounters difficulties when calculating the normal using ϕ . The problem stems from the fact that the truncation errors do not become small around the sharp interface (large gradients) region; strictly speaking one can not even carry out the expansion that leads to (A.9). The mapping improves the results because it introduces factors α and α^2 in η , which facilitate reduction of some of the terms in η . Certainly, one can not affect the second-order curvature terms, γ_x and γ_y , with this mapping, but errors associated with the regular curvature terms, β_x and β_y , as well as the planar terms can be suppressed by using small values of α . Since the curvature terms are normalized by the grid spacing, (A.25), (A.26), and it is presumed that sufficient resolution is utilized in the simulations in order to resolve the spatial and temporal dynamical content, these terms should not take large values and should not affect the resolution of the normals in a properly resolved simulation.

References

- [1] R. Abgrall, How to prevent pressure oscillations in multicomponent flow calculations: a quasi-conservative approach, *J. Comput. Phys.* 125 (1993) 150–160.
- [2] R. Abgrall, S. Karni, Computations of compressible multifluids, *J. Comput. Phys.* 169 (2001) 594–623.
- [3] G. Allaire, S. Clerc, S. Kokh, A five-equation model for the simulation of interfaces between compressible fluids, *J. Comput. Phys.* 181 (2002) 577–616.
- [4] M.R. Baer, J.W. Nunziato, A two-phase mixture theory for the deflagration-to-detonation transition in reactive granular materials, *Int. J. Multiphase Flow* 12 (1986) 861–889.
- [5] G.J. Ball, B.P. Howell, T.G. Leighton, M.J. Schofield, Shock induced collapse of a cylindrical air cavity in water: a Free-Lagrangian simulation, *Shock Waves* 10 (2000) 265–276.
- [6] J.W. Banks, D.W. Schwendeman, A.K. Kapila, W.D. Henshaw, A high-resolution Godunov method for compressible multi-material flow on overlapping grids, *J. Comput. Phys.* 223 (2007) 262–297.
- [7] C.H. Chang, M.-S. Liou, A robust and accurate approach to computing compressible multiphase flow: stratified flow model and AUSM⁺-up scheme, *J. Comput. Phys.* 225 (2007) 840–873.
- [8] I.-L. Chern, J. Glimm, O.A. McBryan, B. Plohr, S. Yaniv, Front tracking for gas dynamics, *J. Comput. Phys.* 63 (1986) 83–110.
- [9] J.-P. Cocchi, R. Saurel, A Riemann problem based method for the resolution of compressible multimaterial flows, *J. Comput. Phys.* 137 (1997) 265–298.
- [10] G. Cochran, J. Chan, Shock initiation and detonation models in one and two dimensions, UCID-18024 (LLNL, 1979).
- [11] O. Desjardins, V. Moureau, H. Pitsch, An accurate conservative level set/ghost fluid method for simulating turbulent atomization, *J. Comput. Phys.* 227 (2008) 8395–8416.
- [12] R.P. Fedkiw, T. Aslam, B. Merriman, S. Osher, A non-oscillatory Eulerian approach to interfaces in multimaterial flows (the Ghost Fluid Method), *J. Comput. Phys.* 152 (1999) 457–492.
- [13] J.B. Freund, R.K. Shukla, A.P. Evan, Shock-induced bubble jetting into a viscous fluid with application to tissue injury in shock-wave lithotripsy, *J. Acoust. Soc. Am.* 126 (2009) 2747–2756.
- [14] J. Glimm, J.W. Grove, X.L. Li, K.M. Shyue, Q. Zhang, Y. Zeng, Three dimensional front tracking, *SIAM J. Sci. Comput.* 9 (1988) 445–473.
- [15] J. Glimm, X. Li, Y. Liu, Z. Xu, N. Zhao, Conservative front tracking with improved accuracy, *SIAM J. Numer. Anal.* 41 (2003) 1926–1947.
- [16] S. Gottlieb, C.W. Shu, Total variation diminishing Runge–Kutta schemes, *Math. Comput.* 67 (1998) 73–85.
- [17] J. Grove, R. Menikoff, The anomalous reflection of a shock wave at a material interface, *J. Fluid Mech.* 219 (1990) 313–336.
- [18] J.-F. Haas, B. Sturtevant, Interaction of weak shock waves with cylindrical and spherical gas inhomogeneities, *J. Fluid Mech.* 181 (1987) 41–76.
- [19] R.K.S. Hankin, The Euler equations for multiphase compressible flow in conservation form: simulation of shock–bubble interactions, *J. Comput. Phys.* 172 (2001) 808–826.
- [20] A. Harten, High resolution schemes for hyperbolic conservation laws, *J. Comput. Phys.* 49 (1983) 357–393.
- [21] X.Y. Hu, B.C. Khoo, N.A. Adams, F.L. Huang, A conservative interface method for compressible flows, *J. Comput. Phys.* 219 (2005) 553–578.
- [22] E. Johnsen, T. Colonius, Implementation of WENO schemes in compressible multi-component flow problems, *J. Comput. Phys.* 219 (2006) 715–732.
- [23] A.K. Kapilla, R. Menikoff, J.B. Bdzil, S.F. Son, D.S. Stewart, Two-phase modeling of deflagration-to-detonation transition in granular materials, *Phys. Fluids* 13 (2001) 3002–3024.
- [24] S. Karni, Multi-component flow calculations by a consistent primitive algorithm, *J. Comput. Phys.* 112 (1994) 31–43.
- [25] S. Karni, Hybrid multifluid algorithms, *SIAM J. Sci. Comput.* 17 (1996) 1019–1039.
- [26] H.O. Kreiss, J. Lorenz, *Initial-Boundary Value Problems and the Navier–Stokes Equations*, Academic Press, New York, 1989.
- [27] S. Kudriakov, W.H. Hui, On a new defect of shock-capturing methods, *J. Comput. Phys.* 227 (2008) 2105–2117.
- [28] P. Lax, B. Wendroff, Systems of conservation laws, *Commun. Pure Appl. Math.* 13 (2) (1960) 217–237.
- [29] R.J. LeVeque, *Finite Volume Methods for Hyperbolic Problems*, Cambridge University Press, New York, 2002.
- [30] T.G. Liu, B.C. Khoo, K.S. Yeo, Ghost fluid method for strong shock impacting on material interface, *J. Comput. Phys.* 190 (2003) 651–681.
- [31] T.G. Liu, B.C. Khoo, K.S. Yeo, An interface interaction method for compressible multifluids, *J. Comput. Phys.* 198 (2004) 35–64.
- [32] T.G. Liu, B.C. Khoo, C.W. Wang, The ghost fluid method for compressible gas–water simulation, *J. Comput. Phys.* 204 (2005) 193–221.
- [33] H. Luo, J.D. Baum, R. Löhner, On the computation of multi-material flows using ALE formulation, *J. Comput. Phys.* 194 (2004) 304–328.
- [34] A. Marquina, P. Mulet, A flux-split algorithm applied to conservative models for multicomponent compressible flows, *J. Comput. Phys.* 185 (2003) 120–138.
- [35] W. Mulder, S. Osher, J.A. Sethian, Computing interface motion in compressible gas dynamics, *J. Comput. Phys.* 100 (1992) 209–228.
- [36] G. Murrone, H. Guillard, A five equation reduced model for compressible two phase flow problems, *J. Comput. Phys.* 202 (2005) 664–698.

- [37] R.R. Nourgaliev, T.N. Dinh, T.G. Theofanous, Adaptive characteristics-based matching for compressible multifluid dynamics, *J. Comput. Phys.* 213 (2006) 500–529.
- [38] R.R. Nourgaliev, T.G. Theofanous, High-fidelity interface tracking in compressible flows: unlimited anchored adaptive level set, *J. Comput. Phys.* 224 (2007) 836–866.
- [39] E. Olsson, G. Kreiss, A conservative level set method for two phase flow, *J. Comput. Phys.* 210 (2005) 225–246.
- [40] E. Olsson, G. Kreiss, S. Zahedi, A conservative level set method for two phase flow II, *J. Comput. Phys.* 225 (2007) 785–807.
- [41] S. Osher, R. Fedkiw, *Level Set Methods and Dynamic Implicit Surfaces*, Springer-Verlag, Berlin, 2003.
- [42] J.J. Quirk, S. Karni, On the dynamics of a shock–bubble interaction, *J. Fluid Mech.* 318 (1996) 129–163.
- [43] R. Saurel, R. Abgrall, A multiphase Godunov method for compressible multifluid and multiphase flows, *J. Comput. Phys.* 150 (1999) 425–467.
- [44] R. Saurel, R. Abgrall, A simple method for compressible multifluid flows, *SIAM J. Sci. Comput.* 21 3 (1999) 1115–1145.
- [45] R. Saurel, F. Petipas, R.A. Berry, Simple and efficient relaxation methods for interfaces separating compressible fluids, cavitating flows and shocks in multiphase mixtures, *J. Comput. Phys.* 228 (2009) 1678–1712.
- [46] J. Sethian, *Level Set Methods and Fast Marching Methods*, Cambridge University Press, Cambridge, 1999.
- [47] K.-M. Shyue, An efficient shock-capturing algorithm for compressible multicomponent problems, *J. Comput. Phys.* 142 (1998) 208–242.
- [48] K.-M. Shyue, A fluid-mixture type algorithm for compressible multicomponent flow with van der Waals equation of state, *J. Comput. Phys.* 156 (1999) 43–88.
- [49] K.-M. Shyue, A fluid-mixture type algorithm for compressible multicomponent flow with Mie Grüneisen equation of state, *J. Comput. Phys.* 171 (2001) 678–707.
- [50] K.-M. Shyue, A wave-propagation based volume tracking method for compressible multicomponent flow in two space dimensions, *J. Comput. Phys.* 215 (2006) 219–244.
- [51] H. Tang, T. Liu, A note on the conservative schemes for the Euler equations, *J. Comput. Phys.* 218 (2006) 451–459.
- [52] H. Terashima, G. Tryggvason, A front-tracking/ghost-fluid method for fluid interfaces in compressible flows, *J. Comput. Phys.* 228 (2009) 4012–4037.
- [53] V.A. Titarev, E.F. Toro, Finite-volume WENO schemes for three-dimensional conservation laws, *J. Comput. Phys.* 201 (2004) 238–260.
- [54] E.F. Toro, M. Spruce, W. Speares, Restoration of the contact surface in the HLL-Riemann solver, *Shock Waves* 4 (1994) 25–34.
- [55] E.F. Toro, *Riemann Solvers and Numerical Methods for Fluid Dynamics*, Springer, Berlin, 1997.
- [56] C.K. Turangan, A.R. Jamaluddin, G.J. Ball, T.G. Leighton, Free-Lagrange simulations of the expansion and jetting collapse of air bubbles in water, *J. Fluid Mech.* 598 (2008) 1–25.
- [57] E. Johnsen, T. Colonius, Numerical simulations of non-spherical bubble collapse, *J. Fluid Mech.* 629 (2009) 231–262.
- [58] W.F. Xie, T.G. Liu, B.C. Khoo, The simulation of cavitating flows induced by underwater shock and free surface interaction, *Appl. Numer. Math.* 57 (2007) 734–745.